Kinetics of Wüstite Formation and Reduction of Manganese alloyed Steel

By

Jie XU

Materials Science and Engineering Department
Delft University of Technology

Abstract

The oxidation and reduction kinetics of a 1.7 wt.% *Mn* steel alloy with 0.1 wt.% *C* was studied in different CO_2/CO mixtures and at different temperatures. The external iron oxide growth, the internal alloying element oxide formation and the reduction of iron oxides were observed with thermogravimetry (TG). The oxidation at 750 ℃ follows a logarithmic growth rate law, which suggests that transport of electrons from the metal through the oxide determines the kinetics. However, the oxidation rate of a linear growth at 950 ℃ obeys a linear growth rate law, which suggests that the dissociation of CO_2 into CO and adsorbed oxygen atoms or ions determines the kinetics. The kinetics of the reduction of external iron oxide by hydrogen follows a First-Order model. A Wüstite scale with internal Manganese oxide was formed during the thermal oxidation in different CO_2/CO mixtures. After reduction with H_2 at 950 ℃, an iron layer with internal Manganese oxide was obtained at the surface of the steel. The depth of the internal Manganese oxide zone increased during the reduction.

Keywords: Manganese alloyed steel, kinetics, oxidation, reduction.

Contents

1. Introduction

Modern Advanced High Strength Steel (AHSS) shows good strength, formability and weldability. To obtain such properties, AHSS is added with several alloying elements (*Mn*, *Al*, *Si*, *Cr* etc.) to enhance the strength while maintaining sufficient ductility. However, the corrosion resistance of these AHSS is usually poor. To protect the AHSS strip against corrosion, it is coated with zinc after passing through annealing furnaces. In the modern manufacturing process, the coating is deposited by hot-dip galvanizing directly after it has passed through annealing furnaces. The annealing and galvanizing line is presented in Figure 1.

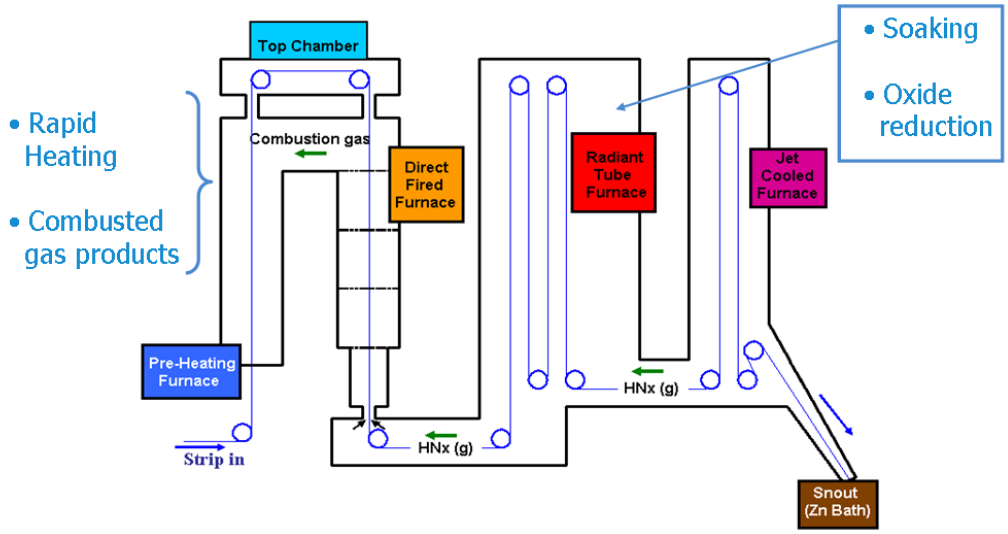

Figure 1 the continuous annealing and galvanizing line

The annealing of the steel strip in most galvanizing lines comprises two subsequent furnace: a Direct Fired Furnace (DFF) and a Radiant Tube Furnace (RTF). The atmosphere in DFF contains almost 20 vol% H_2O and 10 vol% CO_2, which lead to a relatively high oxygen partial pressure. Since the alloying elements have a strong affinity to oxygen, these elements will segregate to the surface and form oxides in DFF. Although the reduction gas ($N_2 + 5$ vol% H_2) flows in the RTF, it only can reduce iron oxide, but not the stable oxides coming from the alloying elements. The oxides of the alloying elements at the surface result in poor wetting with zinc during hot-dip galvanizing or poor adhesion of the zinc coating.

To avoid the formation of external oxidation of the alloying element, the atmosphere in DFF must be adjusted so that external iron oxides form at the surface of the steel strip and the internal alloying element oxides precipitate in sub-surface region of the steel strip as shown in Figure 2 a). Then the external iron oxide is reduced to pure iron in the RTF as shown in Figure 2 b). In this way, the surface of the steel strip is of pure iron, which

can be successfully coated with zinc.

In this master thesis, the kinetics of external iron oxide growth, the internal alloying element oxide formation and the reduction of iron oxides of a Fe-Mn alloy will be studied at different oxygen partial pressures and temperatures. This project will be first step for the research of external and internal oxidation in the multi-element iron alloy.

In this master thesis, a 1.7 wt.% Mn steel alloy with 0.1 wt.% C will be studied about the kinetics of external iron oxide growth, the internal alloying element oxide formation and the reduction of iron oxides of a 1.7 wt.% Mn steel alloy with 0.1 wt.% C will be considered at different temperatures in different gas environments. First the steel alloy is oxidized at 750 ℃, 850 ℃ and 950 ℃ in Ar with CO_2/CO. Next, this oxidized steel alloy is reduced at 750℃, 850℃ and 950℃ in Ar with H_2. In Chapter 2, the theoretical background of alloy oxidation and oxide reduction is outlined. Then, in Chapter 3, the experimental details are described. Further, in Chapter 4, the results of the oxidation and reduction experiments are discussed. In Chapter 5, the conclusions of this research are presented. Finally, in Chapter 错误!未找到引用源。, the recommendations for the future work are offered

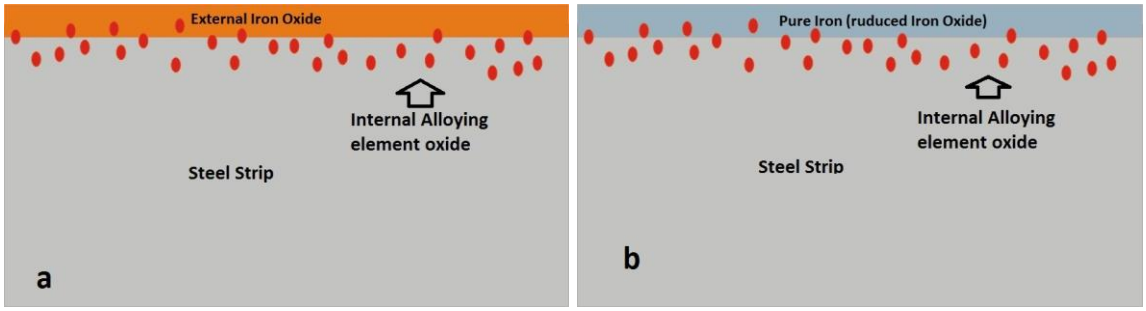

Figure 2 a) Oxidation in the early stage of annealing b) Reduction of iron oxides in the final stage of the annealing process with alloying element oxides in the sub-surface

2. Theories of Oxidation and Reduction

In this chapter, the thermodynamics and mechanisms of alloy oxidation is presented. The thermodynamics of oxidation is considered to select the gas atmosphere (i. e. CO_2/CO ratio) and temperature range. Then, Wagner's theory on the mechanism of alloy oxidation is introduced to predict the experiment results, including the external scale growth rate and the penetration depth of the internal oxides.

2.1 Thermodynamic equilibrium of ideal gases

Ideal gases in an ideal gas mixture behave separately and have no influence on each other. The chemical potential of the ideal gases obeys [1]

$$\mu = \mu^{\circ} + RT\frac{p_i}{p_i^{\circ}} \tag{2.1}$$

$\mu°$ is the standard chemical potential under standard pressure p_i° in a constant temperature. Normally for p_i°, $1atm$ is taken.
Using the Equation (2.1), the partial pressure of oxygen in a CO_2/CO mixture can be calculate considering the following reaction.

$$CO(g)+\frac{1}{2}O_2(g)=CO_2(g) \quad \Delta G^{\circ}=-282420+86.8T(J/mol) \tag{2.2}$$

where ΔG° is the standard Gibbs energy per unite mole.
When the reaction (2.2) is in the chemical equilibrium of the reaction, the Gibbs free energy equals zero:

$$\Delta G=\underbrace{\mu_{CO_2}^{\circ}-\mu_{CO}^{\circ}-\mu_{O_2}^{\circ}}_{\Delta G^{\circ}}+RT\ln\frac{p_{CO_2}}{p_{CO}\,p_{O_2}^{1/2}}=0 \tag{2.3}$$

P_{O_2} is the partial pressure of oxygen.
This equation (2.3) leads to the equilibrium constant k_1 under constant total pressure, which reads

$$k_1=\exp\left(-\frac{\Delta G^{\circ}}{RT}\right)=\frac{p_{CO_2}}{p_{CO}\,p_{O_2}^{1/2}} \tag{2.4}$$

Then, the relationship between CO_2/CO ratio and oxygen partial pressure can be written

$$p_{O_2} = \left(\frac{p_{CO_2}}{p_{CO}}\right)^2 \exp\left(\frac{2\Delta G^\circ}{RT}\right) \tag{2.5}$$

The oxygen partial pressure P_{O_2} as a function of the CO_2/CO for different temperatures, according to Equation (2.5), is plotted in Figure 3.

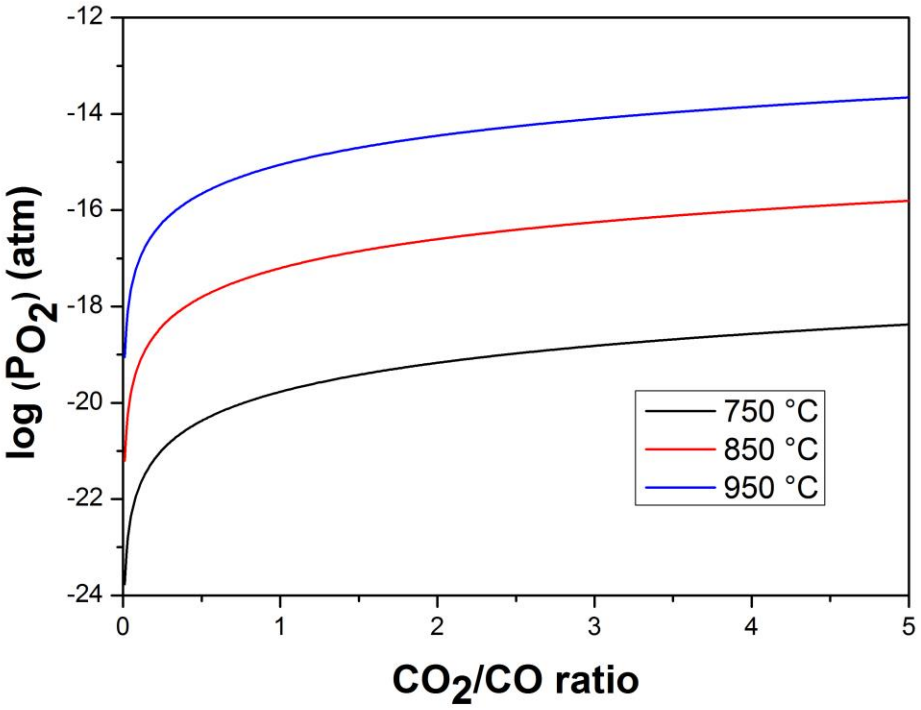

Figure 3: the relationship between partial pressure of oxygen and CO_2/CO ratio in a CO_2 and CO mixture at 750 ℃, 850 ℃, 950 ℃.

2.2 Thermodynamics of metal oxidation

For an oxidation reaction between a metal (M) and oxygen can be written:

$$2M(s) + O_2(g) = 2MO(s) \tag{2.6}$$

The standard free energy of this oxidation reaction is of the form:

$$\Delta G^\circ = -RT \ln\left(\frac{a_{MO}^{\ 2}}{a_M^{\ 2} p_{O_2}}\right) \tag{2.7}$$

where a_M and a_{MO} are the activity of the metal and the oxide. The activity of pure stable solids and liquids are equal to unit, hence

$$p_{O_2} = \exp(\frac{\Delta G^\circ}{RT}) \tag{2.8}$$

Since ΔG° is of the form $\Delta G^\circ = A + BT$, $\log(pO_2)$ has a linear relationship with the reciprocal of the temperature (in Kelvin). Using Equation (2.8), the minimum oxygen partial pressure for forming oxide can be calculated out for each temperature. For example, the oxidation reactions of iron are [2]

$$2Fe + O_2 = 2FeO \quad \Delta G^\circ_{Fe-FeO} = -529780 + 130.8T(J/mol) \tag{2.9}$$

$$6FeO + O_2 = 2Fe_3O_4 \quad \Delta G^\circ_{FeO-Fe_3O_4} = -624420 + 250.2T(J/mol) \tag{2.10}$$

$$4Fe_3O_4 + O_2 = 6Fe_2O_3 \quad \Delta G^\circ_{Fe_3O_4-Fe_2O_3} = -498900 + 281.4T(J/mol) \tag{2.11}$$

Table 1 is the Gibbs free energy and the oxygen partial pressures in the reaction equilibrium at 1000℃.

Reaction	$\Delta G^\circ_{1000℃}$ (J/mol)	p_{O_2} (atm)
$Fe - FeO$	-363272	1.24×10^{-15}
$FeO - Fe_3O_4$	-305915	2.80×10^{-13}
$Fe_3O_4 - Fe_2O_3$	-140678	1.69×10^{-6}

Table 1 Gibbs free energy and the oxygen partial pressures at 1000℃

Thus, when the oxygen partial pressure is less than $1.24 \times 10^{-15} atm$, the pure iron is stable and no iron oxide will form. When the oxygen partial pressure is between $1.24 \times 10^{-15} atm$ and $2.80 \times 10^{-13} atm$, FeO is stable. But, when the oxygen partial pressure is between $2.80 \times 10^{-13} atm$ and $1.69 \times 10^{-6} atm$, Fe_3O_4 will form. When the oxygen partial pressure is larger than $1.69 \times 10^{-6} atm$, only Fe_2O_3 is formed. The stable ranges of the iron oxides for different temperatures and oxygen partial pressures are shown in Figure 4.

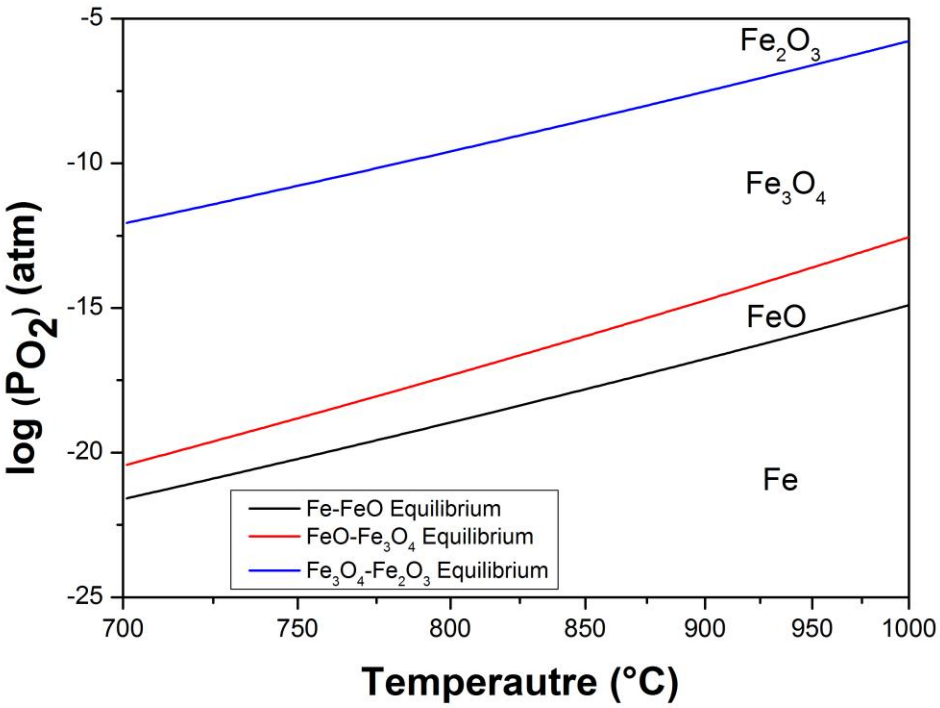

Figure 4 The stable ranges of Wüstite (FeO), Magnetite (Fe_3O_4) and Hematite (Fe_2O_3) as a function of temperature and oxygen partial pressure

2.3 Mechanisms of high temperature oxidation

2.3.1 Defect and oxides types

According to the defect dimension, the defects in the crystal lattice of an oxide can be classified into four types, see Table 2.

Dimension	Name	Example
Zero	Point Defect	Vacancy
One	Line Defect	Dislocation
Two	Planar Defect	Grain boundary
Three	Volume Defect	Pore

Table 2 Defect hierarchy [3]

Metal oxides have mainly two types of point defect: vacancies and/or interstitials. Vacancies are empty lattice sites. Interstitials are atoms that exist at the interstices between the lattice sites. According to the predominant type of the point defect in oxides, the oxides can be divided into two types: n-type oxides and p-type oxides. The charge carriers of n-type oxides are the electrons and on the other hands, holes are the charger carrier in p-type oxide. The different types of oxides have different types of diffusion

mechanisms and different interfacial reactions during the oxidation process. The types of oxides are summarized in Table 3.

Type of oxides	Defect	Charge carriers	Ionic transport	Examples
n-type	Interstitial cations	Electrons	Interstitial	ZnO, CdO
n-type	Anion vacancies	Electrons	Vacancies	Al_2O_3, Fe_2O_3
p-type	Cation vacancies	Holes	Vacancies	NiO, FeO
p-type	Interstitial anions	Holes	Interstitial	UO_2

Table 3 types of oxides [4]

2.3.2 Metal Oxidation mechanisms

The oxidation process can be divided in two stages: the initial oxidation stage and the scale growth stage.
In the initial oxidation stage, a thin oxide film is formed at the surface and the oxidation rate is controlled by transfer of electrons between metal and thin oxide film. The logarithmic equation is derived from this assumption and succeeded in many metals, including *Cu*, *Fe*, *Zn*, *Ni*, *Pb*, *Cd*, *Sn*, *Mn*, *Al*, *Ti*, and *Ta*.
After a relatively thick scale is formed, the metal and oxygen gas are separated by an oxide scale as shown in Figure 5. In this thesis, the internal interface applies to the metal-scale interface and the external interface to the scale-gas interface. The oxidation mechanism is more complex than during the initial stage and comprises four basic steps in the oxidation reaction [5]:

1) Oxygen adsorption on the oxide surface,
2) External interfacial reaction between the adsorbed phase and the oxide phase,
3) Migration of ions, electrons or holes through the oxide scale, and
4) Internal interfacial reaction between the metal and the oxide phase.

These four steps are all possible to be the oxidation rate-determining step.
Here, the electron transfer controlled oxidation and the oxygen-adsorption controlled oxidation (step 1) will be discussed mainly.

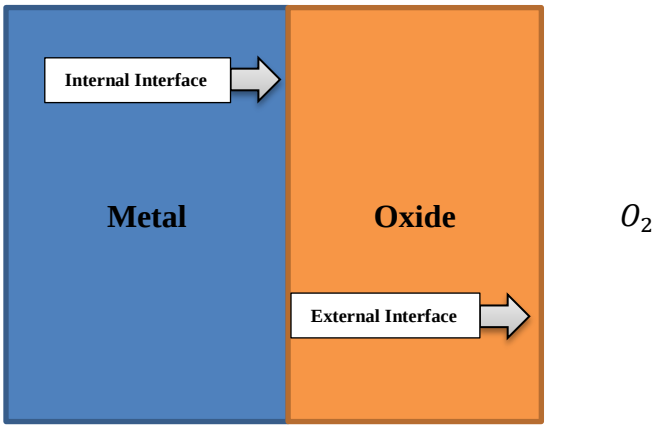

Figure 5 Schematic of the formation of oxide

2.3.3 Interfacial reaction

The interfacial reaction can be classified with four types, depending on the types of oxides and the types of predominant defect as outlined in Table 2. The various oxides have different diffusion mechanisms as well as a different reaction at the interface. The associated defect-reactions for $M + 1/2O_2 = MO$ are shown in Table 3. To describe these defect reactions, the Kröger-Vink notation [6] is used.

Oxide type	Defect	External interface	Internal interface
n-type	Interstitial cations	$\frac{1}{2}O_2 + M_i^{\bullet\bullet} + 2e' \rightleftharpoons O_O^X + M_M$	$M \rightleftharpoons M_I^{\bullet\bullet} + 2e'$
n-type	Anion vacancies	$\frac{1}{2}O_2 + V_O^{\bullet\bullet} + 2e' \rightleftharpoons O_O^X$	$M \rightleftharpoons M_M + V_O^{\bullet\bullet} + 2e'$
p-type	Cation vacancies	$\frac{1}{2}O_2 \rightleftharpoons O_O^X + 2h^{\bullet} + V_M^{''}$	$V_M^{''} + 2h^{\bullet} + M \rightleftharpoons M_M^X$
p-type	Interstitial anions	$\frac{1}{2}O_2 \rightleftharpoons O_i^{''} + 2h^{\bullet}$	$O_i^{''} + 2h^{\bullet} + M \rightleftharpoons M_M^X + O_O^X$

Table 4 Summary of external interfacial reactions and internal interfacial reactions ($M + 1/2O_2 = MO$) [5]

2.3.4 Oxidation in the initial stage

The oxidation rate in the initial stage is controlled by the reaction at the internal interface when thickness of the oxide film is less than hundreds of nanometers. If the oxides have a relatively higher affinity with electron, the oxides will trend to have negative charge and at the same time, the metal will have positive charge at the internal interface. In the reverse case, the oxides will have positive charge and metal will have negative charge. Both of the conditions lead to an electrical double layer at the internal interface. The layer can generate an electric field, which has negative influence on the electric transfer between the metal and the oxide. It is called space-charge effects. As the oxides grow in the initial stage, the space charge effect gets bigger and slows down the electron flow. Further, the oxidation rate decreases. When the oxidation rate is controlled by electron flow between the metal and the oxide, the logarithmic oxidation equation can be derived:

$$y = k_0 \ln(\frac{t}{\tau} + 1) \qquad (2.12)$$

, where y is the thickness of the oxide film and t is time. k_0 and τ are constants.
Since oxidation rate is controlled by the reaction at the internal interface, the oxidation rate is sensitive to the internal interface condition. The oxidation rate in the initial stage is influenced by (1) crystal orientation, (2) lattice transformation, and (3) Curie temperature. [7]

2.3.5 Oxygen adsorption controlled oxidation

When the oxide scale is very thin, the transport ions occur by fast diffusion from the internal interface to the external interface. In this case, the oxygen adsorption will control the whole reaction rate and leads to a linear growth rate behavior. [8] When a high oxygen pressure is required, generally the oxygen gas is directly purged with protection gases. However, when a very low oxygen partial pressure is expected, gas mixtures of CO_2/CO or H_2O/H_2 are used. Many researches have proven that when the oxygen-adsorption controls the whole oxidation reaction rate, the rate is constant and the scale growth is linear with time. [2, 9, 10, 8] For example, in the reaction between CO_2/CO mixture and pure iron to form Wüstite, the oxygen-adsorption reaction can be described as:

$$CO_2(g) + S \underset{k_r}{\overset{k_f}{\rightleftharpoons}} CO(g) + O|S \tag{2.13}$$

where S is the surface adsorption site. K_f and K_r are the forward and reverse rate constant for the reaction. The oxidation rate can be written as

$$Rate = k_f p_{CO_2} \theta_v - k_r p_{CO} (1 - \theta_v) \tag{2.14}$$

Here θ_v is the fraction of available surface sites for the reaction. When the activity of oxygen is equal to that in Fe/FeO equilibrium, the system reaches equilibrium and the net reaction is zero. From Equation (2.4), the equilibrium oxygen activity a_o^* can be expressed as:

$$a_o^* = k_1 \frac{p_{CO_2}}{p_{CO}} \tag{2.15}$$

When substituting Equation (2.15) into Equation (2.14) in net-zero condition, it follows that:

$$k_r (1 - \theta_v) = k_f \theta_v \frac{a_o^*}{k_1} \tag{2.16}$$

Then, Equation (2.14) can be rewritten as:

$$Rate = k_f \theta_v (p_{CO_2} + p_{CO})[N_{CO_2}(1 + \frac{a_o^*}{k_1}) - \frac{a_o^*}{k_1}] \tag{2.17}$$

where $N_{CO_2} = p_{CO_2}/(p_{CO_2} + p_{CO})$. When θ_v and a_o^* are constant values, the oxidation rate will be proportional to the faction of CO_2 and the sum of the pressure of CO_2 and CO at a constant temperature, as has been proven by Pettit et al [8, 9]; see Figure 6 and

Figure 7.

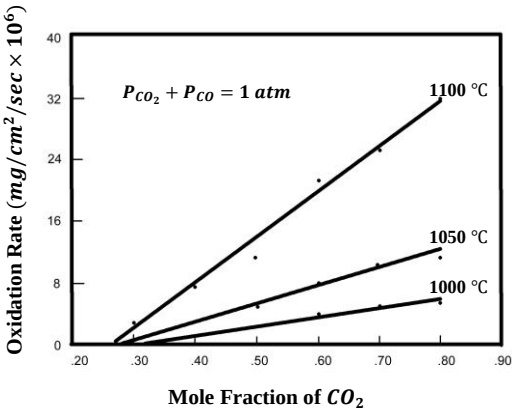

Figure 6 Relationship between the linear rate constant and the mole fraction of CO_2 [8]

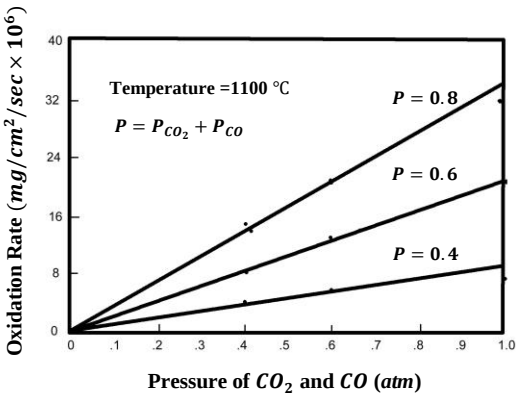

Figure 7 Relationship between the linear rate constant and sum pressure of CO_2 and CO gases [8]

2.4 Oxidation of binary alloy

In the binary alloy M-B, where M is the matrix metal and B is the alloying element, the oxidation reactions can be written as:

$$M + \frac{1}{2}O_2 = MO \quad \Delta G^0_{MO}(T) \tag{2.18}$$

$$B + \frac{v}{2}O_2 = BO_v \quad \Delta G^0_{BO_v}(T) \tag{2.19}$$

When the alloying element B is more active than the metal M ($\Delta G^0_{MO} > \Delta G^0_{BO_v}$), Figure 8 can be obtained from Equation (2.7). In the BO_v stable range, there will is no solvent oxide MO, only the alloying element oxide BO_v. In this rage, two types of oxidation processes can be distinguished for the alloying element , namely: internal oxidation and external oxidation. Internal oxidation is a process, in which the oxygen atoms dissolve into the alloy and diffuse inward to precipitate the alloying element oxide BO_v as shown in Figure 9. When the alloying element diffuses outwards and forms the oxides at the surface of the alloy, the external oxidation occurs.

In the MO stable range, the two elements will oxidize both. However, when the alloying element has a low concentration, the matrix metal is oxidized to form an external oxide scale and the alloying element forms an internal oxide.

In this section, Wagner's theory about the internal oxidation will be introduced and the transition between the internal and external oxidation will be discussed.

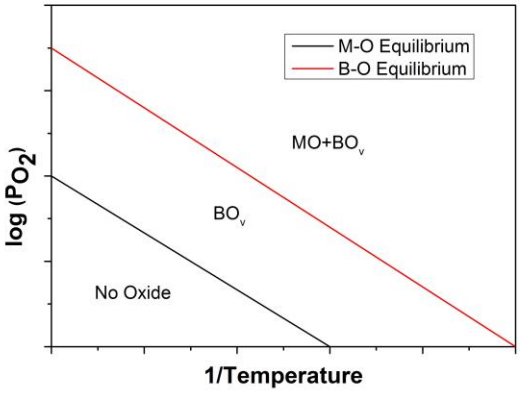

Figure 8 The stable range of the oxides MO and BO_v in the M-B binary alloy

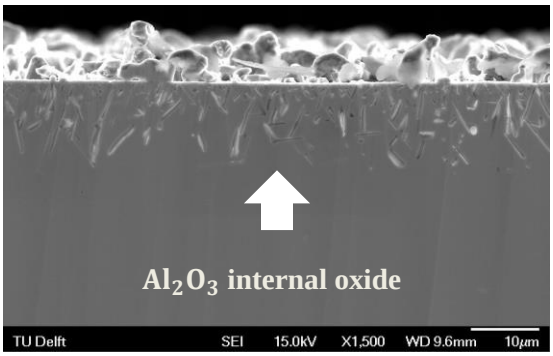

Figure 9 Internal Al_2O_3 in Ni-2.5 at% Al alloy after oxidation at 1100 ℃ in $H_2 + H_2O$ with a dew point of 35 ℃ for 4 hours

2.4.1 Internal oxidation kinetics without external scale

For the internal oxidation, the reaction in the alloy can be written instead of Equation (2.19):

$$B + v\underline{O} = BO_v \tag{2.20}$$

, where $\underline{O}$ is a dissolved oxygen.

$$N_B N_O^v = K_{sp} \tag{2.21}$$

K_{sp} is known as the solubility product. N_O and N_B are the mole fraction of oxygen and alloying element *B*.
In Wagner's general theory [11] , the following three assumptions are made:

1) K_{sp} value is extremely small. In other words, negligible alloying element B is left in the internal oxidation zone (IOZ) and negligible oxygen is dissolved in the alloy.
2) The oxidation reaction only happens at the reaction front x = X_{IOZ} and the mass balance of oxygen and alloying element is achieved.
3) The internal oxidation process is diffusion-controlled, so the depth of the internal oxidation zone (IOZ) increases according to a parabolic kinetics.

$$X_{IOZ}^2 = 2k_p^{(i)}t \tag{2.22}$$

, where $K_p^{(i)}$ is the internal oxidation rate constant.

According to Fick's second law of diffusion, the following equations hold for the concentrations of oxygen and alloying element *B* in the alloy [11].

$$\frac{\partial N_O}{\partial t} = D\frac{\partial^2 N_O}{\partial x^2} \quad \text{for } 0 < x \le X_{IOZ} \tag{2.23}$$

$$\frac{\partial N_B}{\partial t} = D\frac{\partial^2 N_B}{\partial x^2} \quad \text{for } X_{IOZ} \le x \tag{2.24}$$

The boundary conditions are

$$N_O = N_O^{(S)}; x = 0, t > 0$$
$$N_O = 0; x \ge X_{IOZ}, t > 0$$
$$N_B = N_B^{(0)}; x \ge 0, t = 0$$
$$N_B = 0; x \le X_{IOZ}, t > 0$$

$N_O^{(S)}$ is the mole fraction of dissolved oxygen at the surface when the equilibrium is obtained at the gas/scale interface. $N_B^{(0)}$ is the mole fraction of the element B in the bulk alloy.
Then the solutions of the differential Equations (2.23) and (2.24) are respectively:

$$N_O = N_O^{(S)}\left[1 - \frac{erf(x/2\sqrt{D_O t}}{erf(\gamma)}\right] \text{ for } 0 < x \le X_{IOZ} \tag{2.25}$$

$$N_B = N_B^{(O)}\left[1 - \frac{erf(x/2\sqrt{D_O t})}{erf(\gamma\phi^{1/2})}\right] \text{ for } X_{IOZ} \le x \tag{2.26}$$

, where

$$\gamma = (\frac{k_p^{(i)}}{2D_O})^{1/2} \tag{2.27}$$

$$\phi = \frac{D_O}{D_B} \tag{2.28}$$

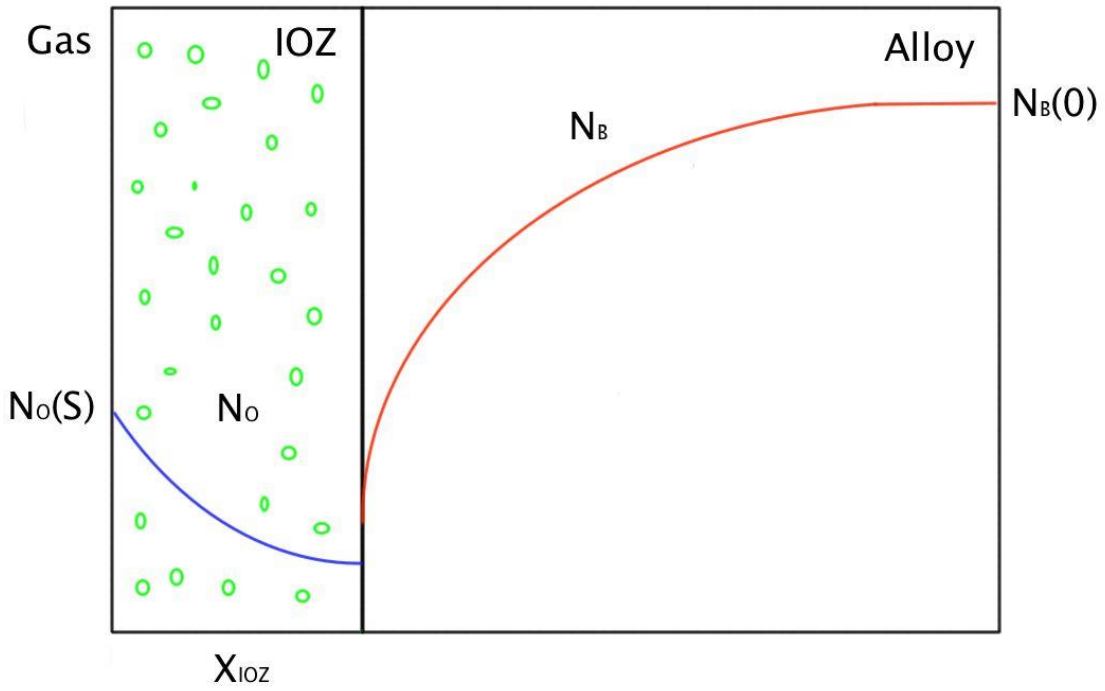

Figure 10 Concentration profile of oxygen and alloying element in the internal oxidation zone of a binary alloy

Considering the mass balance for oxygen and alloying element *B* (cf. second assumption above) at the boundary of the internal oxidation zone and unoxidized alloy, it follows that: Equation (2.29) is obtained.

$$\lim_{\delta\varepsilon\to 0}\left[-D_O\left(\frac{\partial N_O}{\partial x}\right)_{x=X_{IOZ}-\varepsilon} = vD_B\left(\frac{\partial N_B}{\partial x}\right)_{x=X_{IOZ}+\varepsilon}\right] \tag{2.29}$$

Substitution of Equation (2.25) and Equation (2.26) into Equation (2.29) leads to:

$$\frac{N_O^{(S)}}{vN_B^{(0)}} = \frac{\exp(\gamma^2)erf(\gamma)}{\phi^{1/2}\exp(\gamma^2\phi)erfc(\gamma\phi^{1/2})} \tag{2.30}$$

To simplify Equation (2.30), the auxiliary functions $G(x)$ and $F(x)$ are defined as:

$$G(y) = \pi^{1/2} y \exp(y^2) erf(y) \tag{2.31}$$

$$F(y) = \pi^{1/2} y \exp(y^2) erfc(y) \tag{2.32}$$

Then Equation (2.30) becomes:

$$\frac{N_O^{(S)}}{vN_B^{(0)}} = \frac{G(\gamma)}{F(\gamma\varphi^{1/2})} \tag{2.33}$$

This is the relationship between the fraction of the surface dissolved oxygen in the surface and the fraction of alloying element B in the alloy.
Substitution of Equation (2.27) into Equation (2.22) leads to the following equation for the internal oxidation depth, i.e.:

$$X_{IOZ} = 2\gamma\sqrt{D_O t} \tag{2.34}$$

2.5 Mechanism of reduction

The overall reduction reaction of a MO oxide by molecular hydrogen can be presented by:

$$MO(s) + H_2(g) = M(s) + H_2O(g) \tag{2.35}$$

The whole mechanism of the reduction by hydrogen can be divided into two stages: initial stage and growth stage. The initial stage is the beginning of the reduction process, then the reduction gas is in direct contact with the oxide. After forming a metal layer by reduction, the growth stage starts. In this stage, the reduction gases and the oxides are separated by a layer of pure metal.
The detailed reaction in the initial stage can be described as [12]:

$$H_2 \rightleftarrows H(diss) \tag{2.36}$$

$$H(diss) + O(MO) \rightleftarrows H - O(MO) \tag{2.37}$$

$$H(diss) + H - O_{(MO)} \rightleftarrows H - O_{(MO)} - H \rightleftarrows H_2O(diss) \tag{2.38}$$

Firstly, hydrogen gas molecular is aborted on the surface of the oxide. The absorbed hydrogen molecular dissolves into the oxide as hydrogen atoms. And then hydrogen atoms form H-O group with oxygen atom in the oxide. Another dissolved hydrogen atom combines with H-O group to form dissolved water molecular. At last, the water molecular desorbs out form the oxide surface. When hydrogen pressure is extremely low, every step in the initial stage is slower and the initial stage becomes obvious.

After forming a pure metal layer between reduction gases and the oxide, the mechanism of reduction becomes more complex. Since the hydrogen removes the oxygen at the metal-gas interface, an oxygen concentration gradient perpendicular to the surface occurs. The oxygen in metal-oxide interface will diffuse to metal-gas interface, driven by the oxygen gradient. Thus, oxygen vacancies are generated at the metal-oxide interface. The vacancies combine together to form a vacancy cluster or a void at the metal-oxide interface. [13] The cluster or void grows by eliminating vacancies. The excess iron ions

generated by oxygen removing will precipitate out directly on the adjacent metal, leading to the growth of the metal layer. [14]

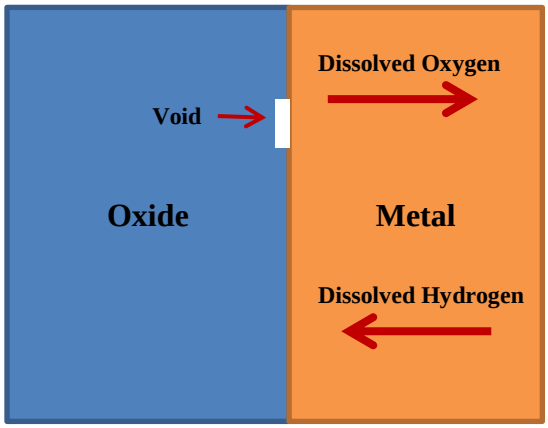

Figure 11 Schematic of the reduction process

During the growth stage, hydrogen gas dissolves in the metal through the reaction:

$$H_2(g) \rightleftarrows 2H(dissolve) \tag{2.39}$$

The dissolved hydrogen atoms diffuse to the metal-oxide interface and react with the oxide. In the reduction of Wüstite, if the reduction reaction occurs at the voids, the water vapour will form through the reaction:

$$FeO(s) + 2H(dissolve) \rightleftarrows Fe(s) + H_2O(g) \tag{2.40}$$

The dissolved hydrogen atoms also recombine to form hydrogen molecular at the void. Then the molecular hydrogen reacts with the oxide directly to form the water vapour. Thus, the gas pressure in the void becomes higher and higher. When the pressure reaches a critical value, the metal layer will burst. [15] The bursting part can be an initiation of the porous iron growth. If the breakdown doesn't occur, the reduction continues by the oxygen diffusion through the metal.

2.6 Kinetics of reduction

The rate of a solid-gas reaction can be generally described by: [16]

$$\frac{d\alpha}{dt} = k(T) f(\alpha) h(P) \tag{2.41}$$

, where α is the conversion fraction and P is the pressure of gaseous product and/or reactants. When the oxide is reduced by hydrogen at a high temperature, water vapour is generated. If the water vapour is removed efficiently from the reaction zone, $h(P)$can be

expressed as:

$$h(P) = P^n \tag{2.42}$$

The influence of the temperature on the reduction kinetics typically can be written with an Arrhenius equation:

$$k(T) = A\exp(\frac{-E}{RT}) \tag{2.43}$$

, where A is the pre-exponential factor and E is the activation energy.
$f(a)$ is decided by the reaction models. The reaction models can be mainly divided to two types: accelerating and decelerating. The accelerating type has lowest reaction rate at the beginning of the reaction and the rate continuously increase with increasing the conversion fraction. At the end of the reaction, the rate reaches the highest value. This model can be expressed by a Power-Law model:

$$f(\alpha) = n\alpha^{(n-1)/n} \tag{2.44}$$

The decelerating type has maximum reaction rate at the beginning of the reaction and the rate is continuously reducing while the conversion fraction increases. The model can represent by a Reaction-Order model:

$$f(\alpha) = (1-\alpha)^n \tag{2.45}$$

The typically used models are summarised in Table 5. More solid state models and the derivations can be found in Khawam and Flanagan's review article. [17]

Reaction model	**Differential form** $\boldsymbol{f(\alpha) = k(T)da/dt}$	**Integral form** $\boldsymbol{g(\alpha) = k(T)t}$
Power law	$2\alpha^{1/2}$	$2\alpha^{1/2}$
Power law	$3\alpha^{2/3}$	$\alpha^{1/3}$
Power law	$4\alpha^{3/4}$	$\alpha^{1/4}$
Zero-order	1	α
First-order	$(1-\alpha)$	$-\ln(1-\alpha)$
Second-order	$(1-\alpha)^2$	$1/(1-\alpha) - 1$
Third order	$(1-\alpha)^3$	$(1/2)[(1-\alpha)^{-2} - 1]$

Table 5 some kinetic models used in the solid-state kinetics

3. Experimental

In the oxidation experiment with the 1.7 wt%Mn steel alloy, a Wüstite (*FeO*) scale with internal MnO oxide is expected. In the reduction experiments with the steel alloy, the reduction gas should remove the whole Wüstite scale to form a pure iron layer at the surface of the samples.
In this chapter, the experimental procedures are described, including the gas composition used in the oxidation and reduction experiments. Also the thermogravimetric method used to observe the oxidation and reduction kinetics will be addressed. Finally, the methods used to characterize the composition and microstructure near the surface of the steel alloy after oxidation as well as after reduction are as well as the methods to characterize are discussed.

3.1 Sample preparation

Cold rolled sheet of Fe-1.7 wt% Mn with 0.1 wt% C from TATA Steel is used in the experiments. The This sheet was cut into disk-shaped samples with 10 mm diameter and 1 mm thickness by Spark erosion. Next, the samples are mechanically grinded with Silicon Carbide emery papers from grade 600 to grade 4000.

3.2 Oxidation experiment

In the oxidation experiment, pure Wüstite is the desired oxide which is formed by oxidizing in a CO_2/CO mixture. According to Figure 3 and Figure 4, the gas compositions and temperatures are indicated in Table 6 and Figure 12.

Ratio\Temperature	**750** ℃	**850** ℃	**950** ℃
$\boldsymbol{CO_2/CO = 1}$	2 hours	2 hours	2 hours
$\boldsymbol{CO_2/CO = 2}$	2 hours	2 hours	2 hours
$\boldsymbol{CO_2/CO = 3}$	2 hours	2 hours	2 hours

Table 6 the oxidation experiment conditions

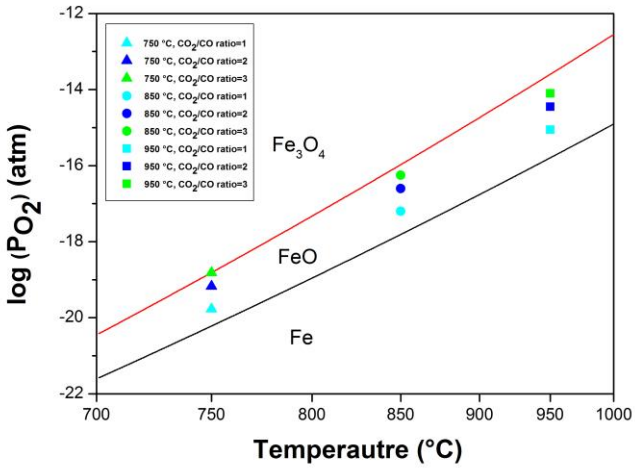

Figure 12 The $CO_2 + CO$ gas compositions and the temperatures in the oxidation experiments

The oxidation experiments were carried out with thermogravimetric analysis (TGA) using a Setaram Evoluation 1750. The TGA conditions are shown in Table 7. When heating up the furnace of the TGA with the sample, 15 ml/min $H_2 + Ar$ is purged into the furnace tube to remove possible oxides and prevent oxidation of the sample. When cooling down the furnace after the oxidation, the furnace is purged with pure Ar to protect the oxides.

3.3 Reduction experiment

The reduction is performed with TGA using the conditions specified in Table 7. In the reduction experiments, first the oxidation of the sample is carried out; see Section 3.2. Next, the oxides formed are reduced by 15 vol% H_2 at the same temperatures as the oxidation experiments. The time of the reduction experiment is 2 hours or 4 hours.

TGA parameters	
Total gas pressure	~960 mbar
Total gas flow	100 ml/min
Gas flow of $CO_2 + CO$ (Oxidation)	60 ml/min
Gas flow of H_2 (Reduction)	15 ml/min
Carrier gas	Ar
Gas flow speed	0.67 cm/s
Temperature increasing rate	15 ℃/min
Temperature decreasing rate	15 ℃/min

Table 7 TGA parameters

3.4 Instruments

Termogravimatric Analyzer (TGA)

The oxidation and reduction experiments are performed by the thermogravimatric analyzer: *SETARAM evolution 1750*. The structure of TGA is shown in Figure 13. The sample is in the central of the furnace. When the oxidation or reduction reaction occurs, a high-sensitive balance at the top of TGA measures the weight change of the sample during the experiment. The resolution of the balance is 0.03 μg.
The gas atmosphere in the furnace is controlled by the flows rates of the carrier gases and auxiliary gasses. The flows are controlled by the gas flow controller: *Brankhorst EL-FLOW*. The errors of the flow controller are listed in Table 8.

Gases	Expected flow rate ± Error	Gases	Expected flow rate ± Error
Ar	40 ± 0.4 ml/min	***CO_2***	45 ± 0.425 ml/min
H_2	15 ± 0.09 ml/min	***CO***	15 ± 0.275 ml/min
CO_2	30 ± 0.35 ml/min	***CO***	20 ± 0.3 ml/min
CO_2	40 ± 0.4 ml/min	***CO***	30 ± 0.35 ml/min

Table 8 Desired flow rates and the errors in TGA

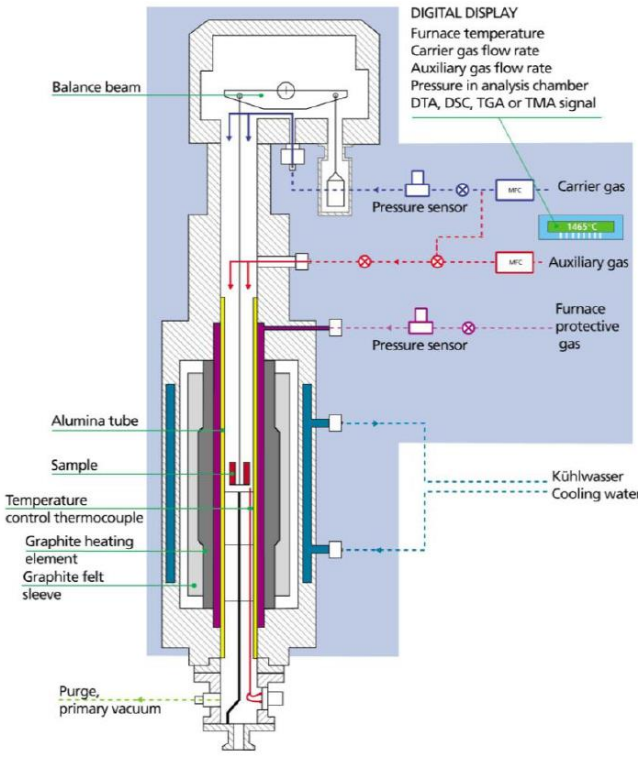

Figure 13 Structure of the termogravimatric analyzer

X-ray diffractometry (XRD)

X-ray diffractometry (XRD) is a widely used method in the characterization of crystal materials. The theory of XRD is based on the Bragg's Equation:

$$n\lambda = 2d\sin\theta$$

, where n is an integer, λ is the wavelength of the radiation, d is the spacing of the crystal lattice planes, and θ is the angle, which the incident beam makes with the lattice planes. Since different materials have different the spacing of the crystal lattice planes d, every material has the peak at different angle θ. Every crystal material has several diffraction planes, so several peaks can be found from a components.

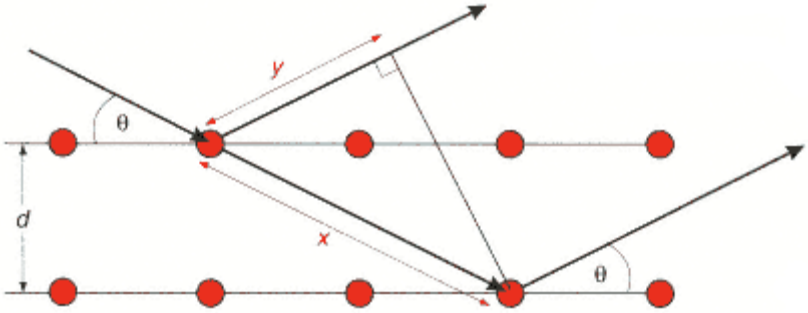

Figure 14 Schematic representation of X-ray diffraction in a crystal lattice

In this thesis, XRD is performed by *Bruker D8 advance* diffractometer with *Vantec* position sensitive detector. The diffractometer uses $Co\ K_\alpha$ radiation with a wavelength 1.790260 Å.

Ion Polishing

Ion polishing is used to obtain a high quality and clean cross-section for SEM and EPMA. As shown in Figure 15, the ion beam is generated by *Ar* ion gun. Firstly, the ion beam removes shield plate. Next, a thin layer of the sample is removed by the ion gun.

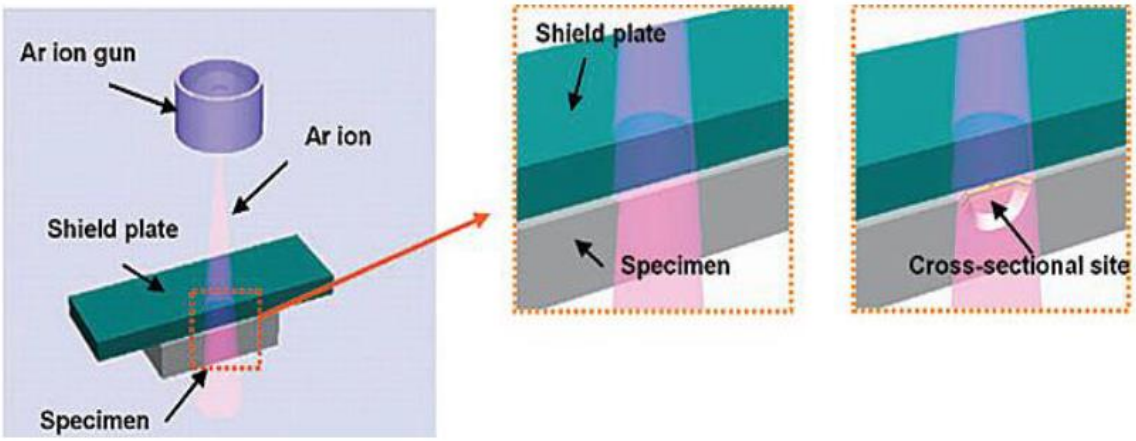

Figure 15 Ion polishing process

In this thesis, *Joel SM-09010* is used to polish the sample. To protect the surface of the sample, 1 μm pure *Cr* is coated on the surface by *Leica EM SCD 500*. Then, a silicon wafer is fixed on the surface with Resin and Hardener. Finally, the sample is polished with ion accelerating voltage 4 *kV* for 16 hours.

Scanning Electron Microscopy (SEM)

The primary electron beam of Scanning Electron Microscopy interacts with the sample and generates several signals: secondary electrons, back-scattered electrons, and X-ray photons.

Secondary electrons are produced as a result of the incident primary electron beam's interaction with the electrons of atoms in the sample. Since the interaction occurs near to the surface of the sample, second electrons provide information about the surface topography of the sample. A high resolution image of the surface can be obtained from secondary electrons.

Back-Scattered Electrons (BSE) are essentially primary incident elections that turn back from a specimen due to large angle scattering. The proportion of back-scattered electrons will depend on the average atomic number of the specimen. Thus, BSE can provide information on the topographic and atomic contrast of the sample.

X-ray photons are generated by the interaction of the incident primary electrons with the inner-shell electrons of the atoms in the sample. Since the incident electrons generate secondary electrons from the inner shell, an electron vacancy is created at a lower energy shell. Electrons from a higher energy shell drop to the electron vacancies, generating X-ray photons. X-ray photons are used to characterize the elements in the sample, namely Energy-dispersive X-ray Spectroscopy (EDS).

Here, Scanning Electron Microscopy *Joel JSM 6500F* is used to perform SEI, BSE and EDS analysis. EDS uses *ThermoFisher UltraDry* as the detector.

Electron Probe Microanalyzer (EPMA)

Electron probe Microanalyses (EPMA) has a same theory with EDS. However, EPMA is able to acquire more precise, quantitative elemental analyses at very small sport size.

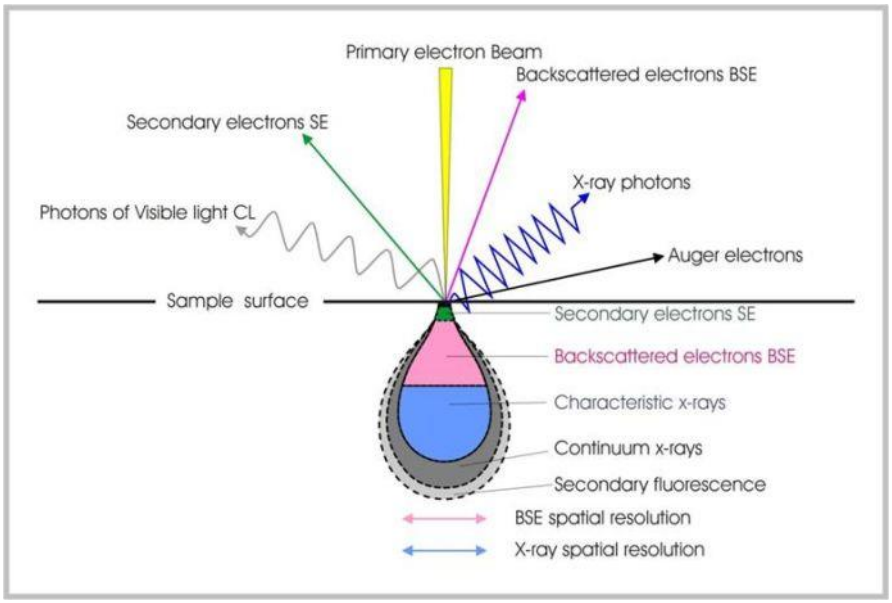

Figure 16 the generated signals by primary electron beam

4. Experiment Result & Discussion

In this chapter, the results of the oxidation experiments and the reduction experiments with 1.7 wt% Mn steel are discussed. In the oxidation experiments, the oxidation products and the rate controlling factors are described. Then, the depths of the internal oxide zone are compared with the calculated values. For the reduction experiments, a Fist-Order model is used to describe the reduction process. Next, the mechanism of the reduction of *FeO* is discussed. Finally, the Manganese distributions and the internal oxidation depths after the reduction are also mentioned in this chapter.

4.1 Oxidation experiment result & discussion

Since the oxidation experiments are performed in the range where Wüstite (*FeO*) is stable, an *MnO* internal oxidation with Wüstite external scale is expected. In this section, the oxidation product, the morphology and the rate controlling factors of Wüstite growth are described. Also the internal oxidation and the distribution of alloying element *Mn* are discussed.

4.1.1 Oxidation product

Wüstite is the expected product in the oxidation experiments. EPMA and XRD are used to analyze the oxidation products. The XRD results (Appendix A) are summarized in Table 9.

Experiment temperature	CO_2/CO ratio	XRD identification
750 ℃	CO_2/CO ratio =1	Wüstite with some Magnetite
750 ℃	CO_2/CO ratio =2	Wüstite with some Magnetite
750 ℃	CO_2/CO ratio =3	Wüstite with some Magnetite
850 ℃	CO_2/CO ratio =3	Wüstite with some Magnetite
950 ℃	CO_2/CO ratio =3	Wüstite with some Magnetite

Table 9 XRD analysis results of the oxidation products

XRD results in Table 9 show that next to Wüstite also Magnetite (Fe_3O_4) is one of the oxidation products. However, according to Figure 12, all the CO_2/CO compositions are in Wüstite stable range. Thus, most of the Magnetite is formed during the cooling process after the experiments.

As shown in the iron-oxygen equilibrium diagram (Figure 17), Wüstite is not stable below 560 ℃. After the formation of Wüstite during the oxidation at high temperatures, the samples were cooled down by 15 ℃/min. When the temperature is lower than the red line in Figure 17, Magnetite will precipitate out. Thus, Magnetite exists in the Wüstite as a precipitate. The starting temperature of Magnetite precipitation depends on the non-

stoichiometric deviation of Wüstite. Since the reduction experiments were executed directly after the oxidation experiments (i.e. without the cooling process), the oxide scale consist of high pure Wüstite in this case.

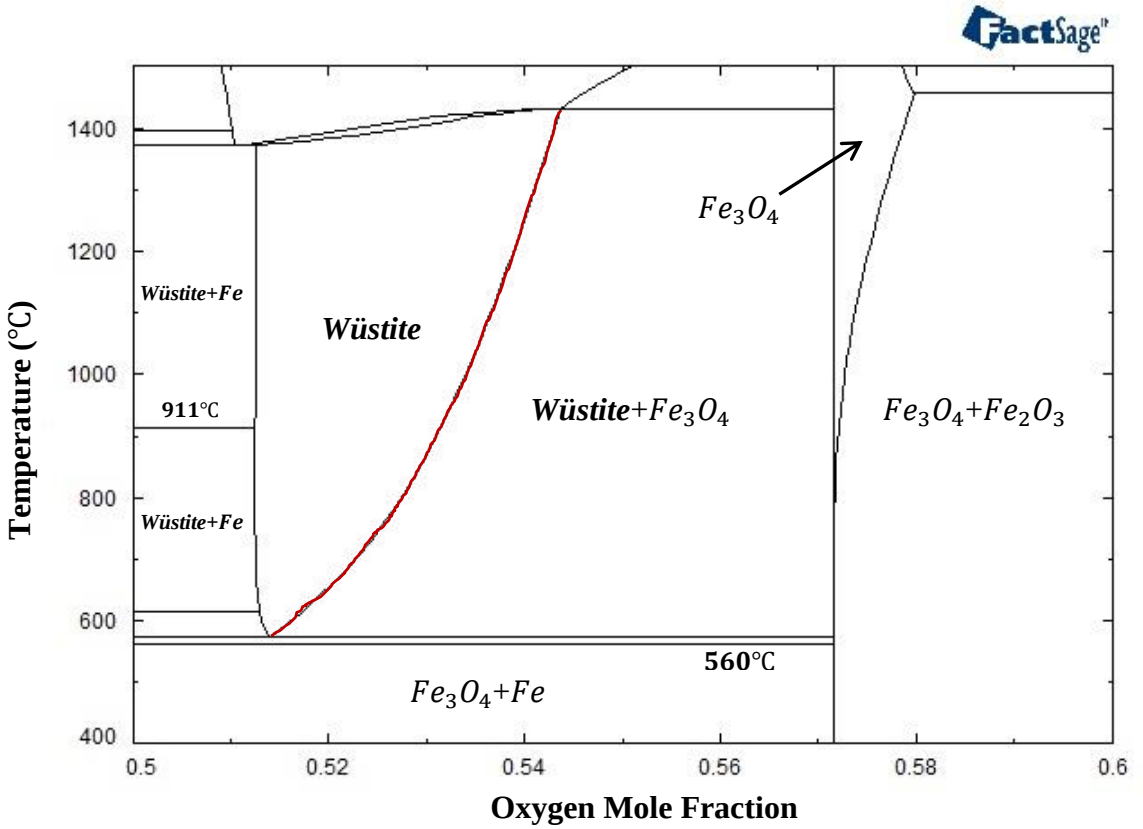

Figure 17 Iron-Oxygen phase diagram from FactSage

4.1.2 Oxide morphology

The surface images of the samples oxidized in CO_2/CO ratio= 2 at different temperatures are shown in Figure 18. The oxides formed at 950 ℃ have a larger particle size than oxides formed at 750 ℃ and 850 ℃. Furthermore, another nucleation starts on the surface of oxide particles at 950 ℃.

For the samples with lower oxide rates, the oxides do not fully cover the surface of the samples as shown in Figure 18-(4). Only the samples oxidized at 950 ℃ in CO_2/CO ratio= 2 and CO_2/CO ratio= 3 have continues oxide layers. Thus, here the oxidation rates and the reduction rates both are average values. The characterization of the surface and the cross-section is performed at the oxide-covered range.

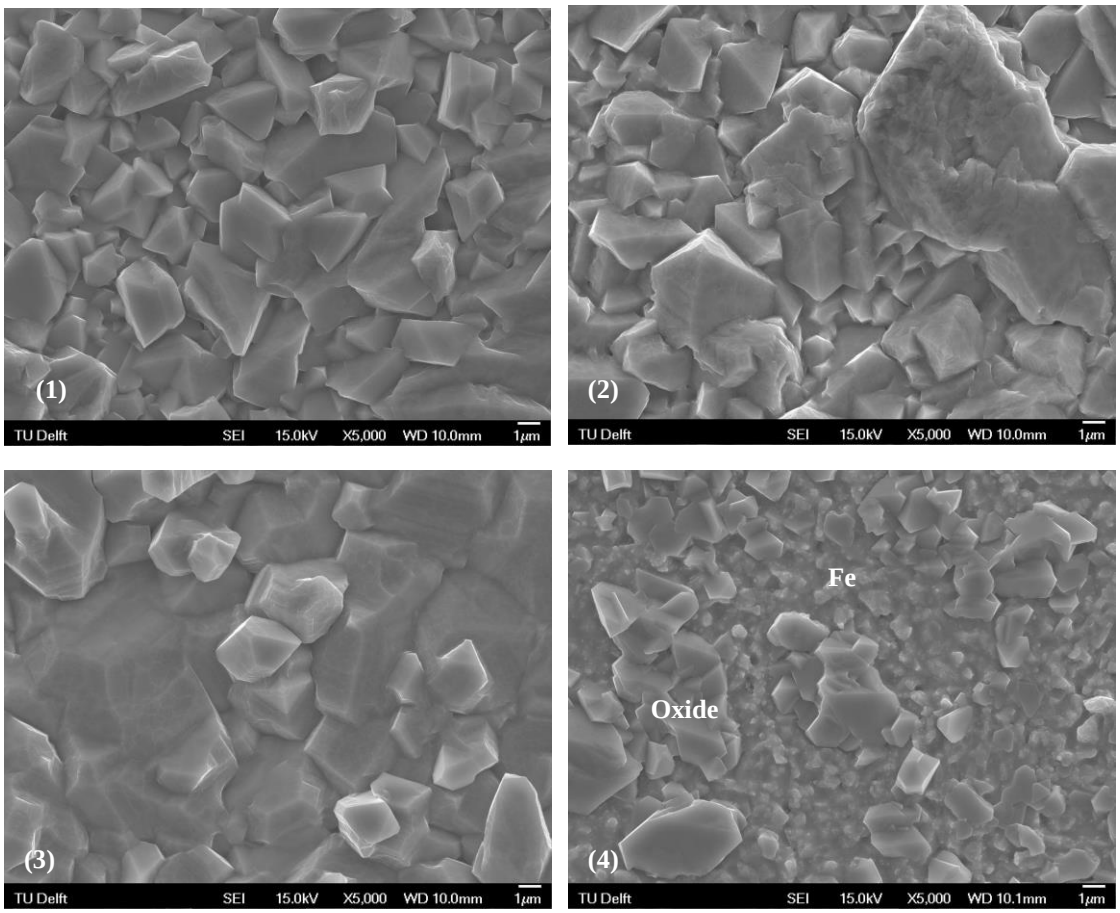

Figure 18 SEM images of the surfaces of the samples oxidized in CO_2/CO ratio= 2 at different temperatures (1) 750 ℃ (2) 850 ℃ (3) 950 ℃ (4) 750 ℃

4.1.3 Kinetics of Oxidation

Two types of oxide growth kinetics were observed in the oxidation experiments, namely: (1) logarithmic and (2) linear growth. During the oxidation at 750 ℃, the weight gain starts according to a logarithmic growth rate law and followed by a linear relation with time as shown in Figure 19 and Figure 20. In the logarithmic growth rate regime, the oxidation rate is controlled by electron transport from the metal to the oxide; see Section 2.3.4. When the weight gain is 0.025~0.050 mg/cm^2 at 750 ℃, the transition from logarithmic to the linear growth occurs. However, in the oxidation experiments, the oxides do not fully covered the surface, so the critical thickness of the transition can not be calculate from the weight gain.

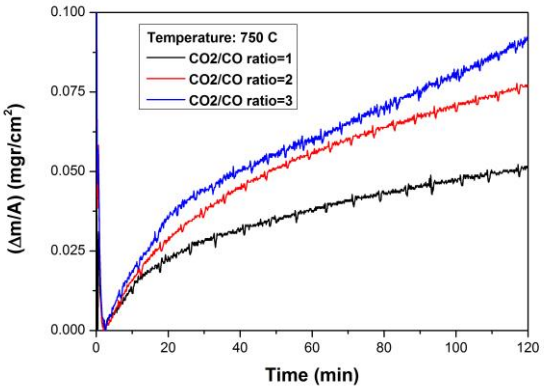

Figure 19 The weight gains as function of the time for Fe-1.7wt% Mn alloy oxidized at 750 ℃ in different CO_2/CO ratios

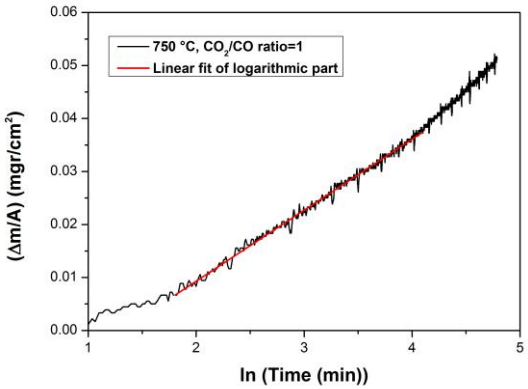

Figure 20 The weight gains as function of the logarithm of time for Fe-1.7wt% Mn alloy oxidized at 750 ℃ in CO_2/CO ratio= 1

During oxidation at 850 ℃ and 950 ℃, linear growth is predominant with a very short time of logarithmic growth as shown Figure 21.

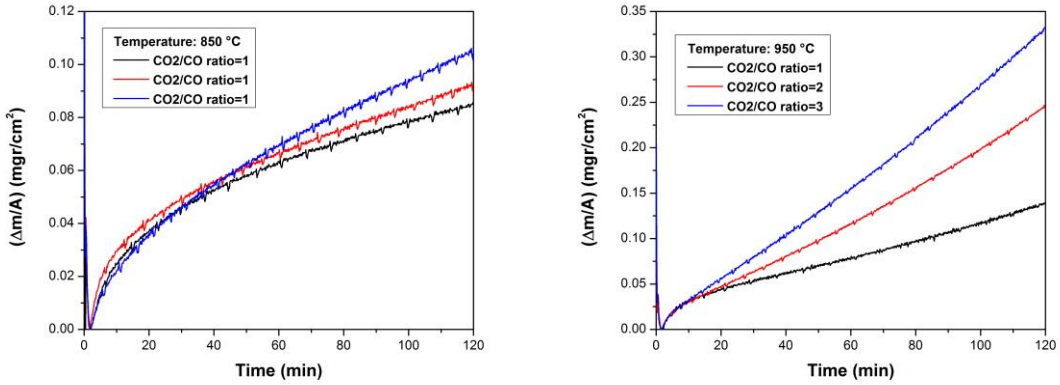

Figure 21 The weight gains as function of time in the oxidation at 850 ℃ and 950 ℃

The oxidation rates for the linear growth regions in the oxidation experiments are summarized in Table 10. Equation (2.17) can be applied to the oxidation rates at 950 ℃ as shown in Figure 22. Thus, the dissociation of CO_2 into CO and adsorbed oxygen atoms or ions is here the rate-controlling process when the oxidation at 950 ℃; see Section 2.3.5. However, Equation (2.17) is just applicable at the temperature 925 ℃-1075 ℃ [9]. The oxidation below 900 ℃ has a different activation energy and no models are found to explain it. The data for the growth kinetics at 750 ℃ and 850 ℃, are insufficiet to derive a new reliable model.

Ratio\Temperature	**750** ℃ ($\times 10^{-4} mg/cm^2$)	**850** ℃ ($\times 10^{-4} mg/cm^2$)	**950** ℃ ($\times 10^{-4} mg/cm^2$)
$\mathbf{CO_2/CO = 1}$	1.98	3.44	4.86
$\mathbf{CO_2/CO = 2}$	4.04	4.82	6.72
$\mathbf{CO_2/CO = 3}$	8.21	22.60	29.15

Table 10 The average oxidation rates of the linear growth parts at 750 ℃, 850 ℃ and 950 ℃

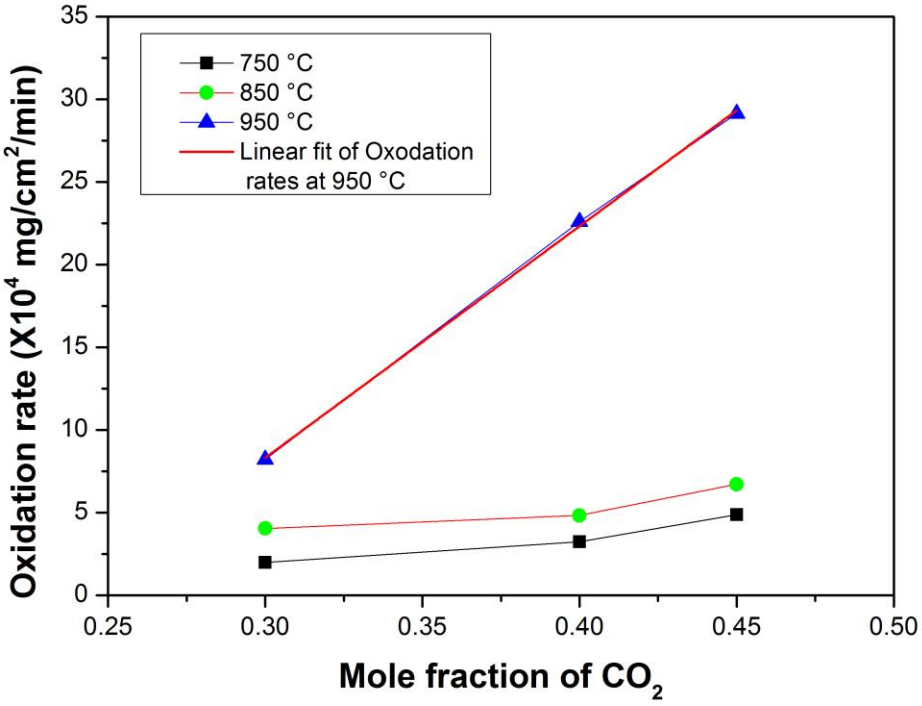

Figure 22 Dependence of the oxidation rates on the mole fractions of CO_2 in a CO_2/CO gas mixture at 750 ℃, 850 ℃ and 950 ℃

4.1.4 Internal oxidation in oxidation

Since the oxidation experiments with 1.7 wt%Mn steel are performed in the temperature and oxygen partial pressure range where Wüstite is stable, a Wüstite scale with a MnO internal oxide zone is expected. The cross-section images and EPMA results of the sample oxidized at 950 ℃ in CO_2/CO ratio equal to 3 are shown in Figure 23.

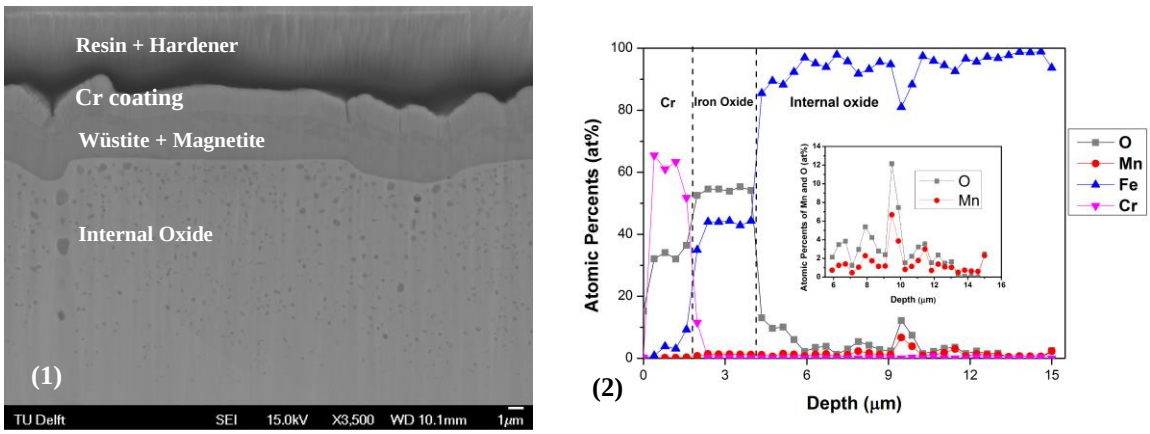

Figure 23 The cross-section and EPMA result of the sample oxidized at 950 ℃ in CO_2/CO ratio equal to 3

The layer of iron oxide and the internal oxidation zone are clearly visible in Figure 23-(1). The EPMA result in Figure 23-(2) indicates that the external scale is iron oxide and the internal oxide is manganese oxide. In the internal oxide zone, most of the internal oxide particles are less than the size of the scattered electron in EPMA (0.6~0.8 μm). Thus, every data point in the EPMA includes iron around particles. The actual concentration of manganese and oxygen in the internal oxide should be much higher than the detected value in Figure 23-(2).

The depth of the internal oxide zone is summarized in Table 11. The depth values are all from the region covered by the external scale. The internal depths at a same temperature in different gas mixtures have an equal value in the error range. Thus the oxygen fraction $N_O^{(S)}$ at the internal interface in Equation (2.30) is determined by $Fe\text{-}O$ Equilibrium, instead of $CO_2\text{-}CO$ equilibrium. Using Equation (2.30) and (2.34) in Wagner's theory; see Section 2.4.1, the depth of the internal oxide is calculated out and present in Table 11. The data used in the calculations are listed in Appendix B.

Ratio\ Temperature	$\mathbf{CO_2/CO = 1}$ **(μm)**	$\mathbf{CO_2/CO = 2}$ **(μm)**	$\mathbf{CO_2/CO = 3}$ **(μm)**	**Calculated depth (μm)**
750 ℃	3.18	2.70	2.40	1.17
850 ℃	11.62	12.09	12.33	9.34
950 ℃	16.18	16.18	16.79	8.21

Table 11 The depth of internal oxidation zone after oxidation of 1.7 wt%Mn steel compared with the calculated depth

The depths of internal oxide zone are larger than the calculated values, but the values are in the same order of magnitude. Wagner's theory does not account for the diffusion of oxygen enhanced by the grain and phase boundaries. The diffusion coefficients of manganese and oxygen in iron used in the calculation hold for bulk diffusion. In the oxidation, the oxides precipitate out along the grain boundaries as shown in Figure 24. Since the grain boundary can accelerate the element diffusion, a higher depth of the internal oxidation zone than can be expected when comparing with only bulk diffusion.

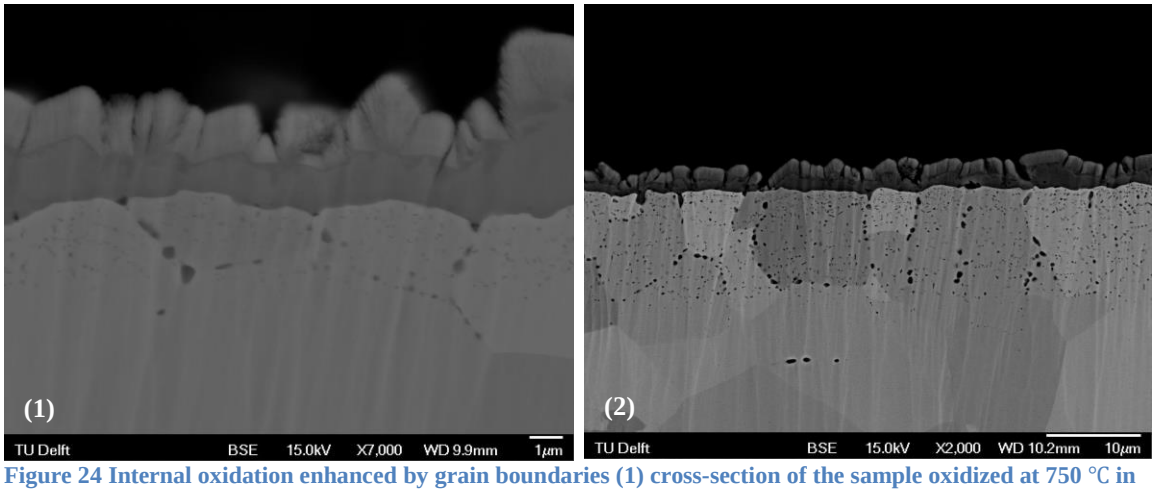

Figure 24 Internal oxidation enhanced by grain boundaries (1) cross-section of the sample oxidized at 750 ℃ in

$CO_2/CO = 2$ (2) cross-section of the sample oxidized at 850 ℃ in $CO_2/CO = 2$

4.1.5 Mn distribution

Manganese has strong affinity with oxygen. During the oxidation experiment, manganese atoms diffuse to the surface of the samples as shown in Table 12. Thus, the scales are not the oxide layers, containing Manganese element. The XRD result (Appendix A) do not indicate any Manganese oxide. Thus, the manganese exists in the scale as a solid solute instead of manganese oxide particles or layers. The values in Table 12 are the average values obtained from a series of analysis.

Experiment	Mn concentration (*at%*)
750 ℃, CO_2/CO ratio=2	2.79
750 ℃, CO_2/CO ratio=3	1.94
850 ℃, CO_2/CO ratio=1	5.9
850 ℃, CO_2/CO ratio=2	2.98
950 ℃, CO_2/CO ratio=1	2.68
950 ℃, CO_2/CO ratio=2	1.6
950 ℃, CO_2/CO ratio=3	0.925

Table 12 Manganese concentrations at the surface of the samples after the oxidation experiments from X-ray micro analysis

4.2 Reduction experiment result & discussion

In this section, the microstructures observed at the surface and in the cross-section of the 1.7 wt% Mn steel samples after reduction are described. Next, a First-Order model is used to describe the reduction process. At last, the internal oxidation depth is discussed.

4.2.1 Surface and Cross-section of samples after the reduction

The surfaces and cross-sections of some samples after the reduction are shown in Figure 25. The surfaces of the samples in Figure 25 have high-purity iron with less than 3 at% *Mn* as determined with X-ray microanalysis. No oxide is found on the surface. The cross-section in Figure 25-(1) shows that large manganese oxide precipitates are formed under the reduced layer. Figure 25-(3) shows that voids are generated during the reduction process, which is in agreement with the reduction mechanism proposed in Section 2.5. both large manganese oxide precipitates and voids are seen. The mechanism for the formation of large manganese oxide precipitates will be discussed in Section 4.2.4.

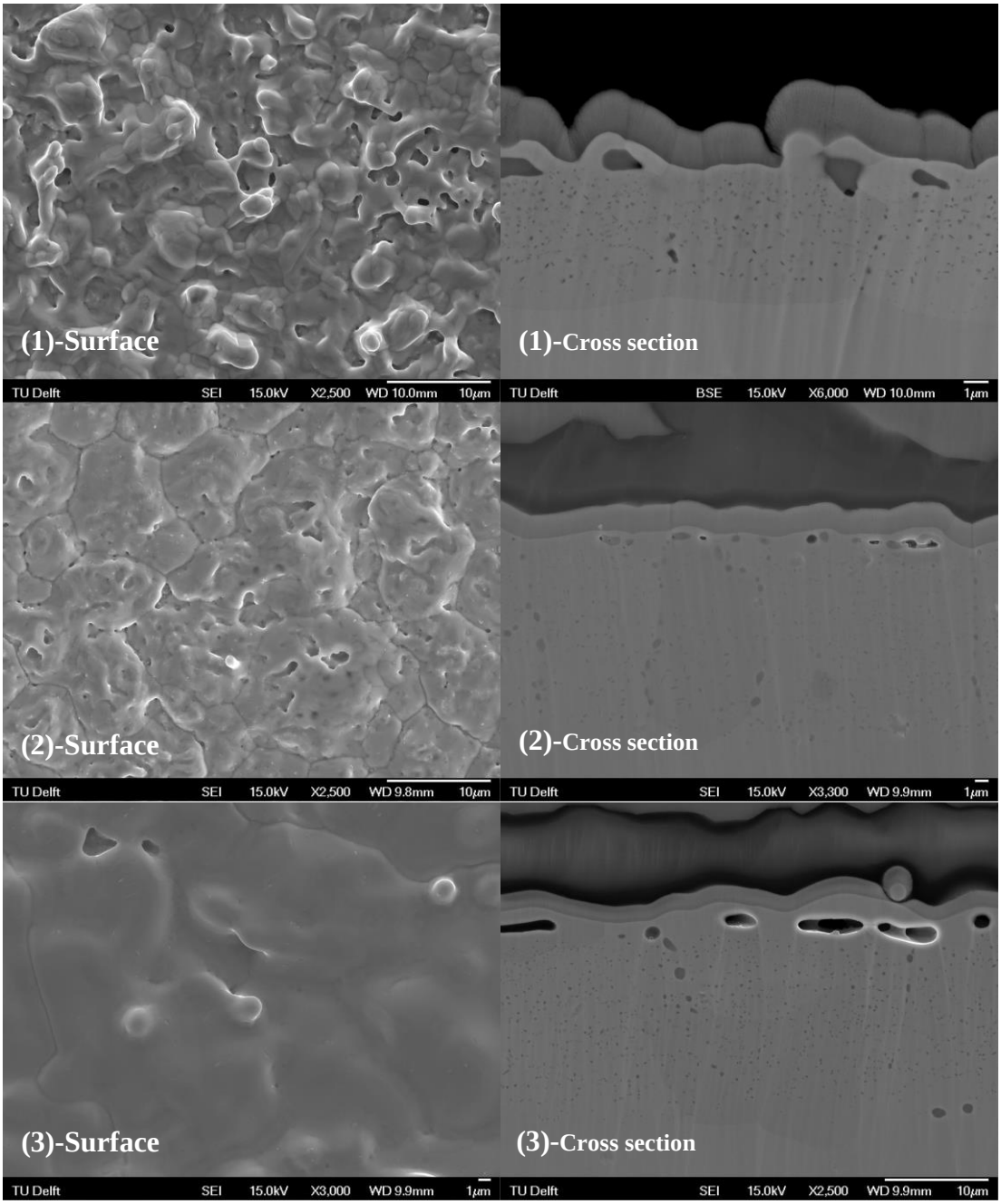

Figure 25 Surface and cross-section of the samples after the reduction (1) the sample oxidized in $CO_2/CO = 3$ at 750 ℃ and reduced in 15 vol% H_2 at 750 ℃ (2) the sample oxidized in $CO_2/CO = 3$ at 850 ℃ and reduced in 15 vol% H_2 at 850 ℃ (3) the sample oxidized in $CO_2/CO = 3$ at 950 ℃ and reduced in 15 vol% H_2 at 950 ℃

4.2.2 Kinetics of Reduction

The weight change during the reduction experiments are shown in Figure 26. The reduction rate is extremely fast at the beginning. Then, the reduction rate continuously decreases. After a certain time, the weight decrease becomes stable, but does not cease at

the end of the experiments. However, the XRD results (Appendix A) show that all the iron oxides were removed during reduction. The cross-section image and EPMA results (Figure 27) of the sample, which were oxidized in $CO_2/CO = 3$ at 950℃ and then reduced for 2 hours with 15 vol% H_2, shows that no iron oxides are left on the surface of the samples after the reduction. However, the weight is still reducing after 2 hours in Figure 26-(4). Thus, the weight decreasing between 120 min and 240 min is not caused by oxide reduction. The samples only contain 4 elements: *Fe*, *Mn*, *O*, *C*. Figure 28 proves that the decarburization of the steel occurs during the reduction process. In Figure 28, the original sample after annealing has much more pearlite (black part) than the sample after the reduction experiment. Thus, during the reduction process, carbon is removed by hydrogen.

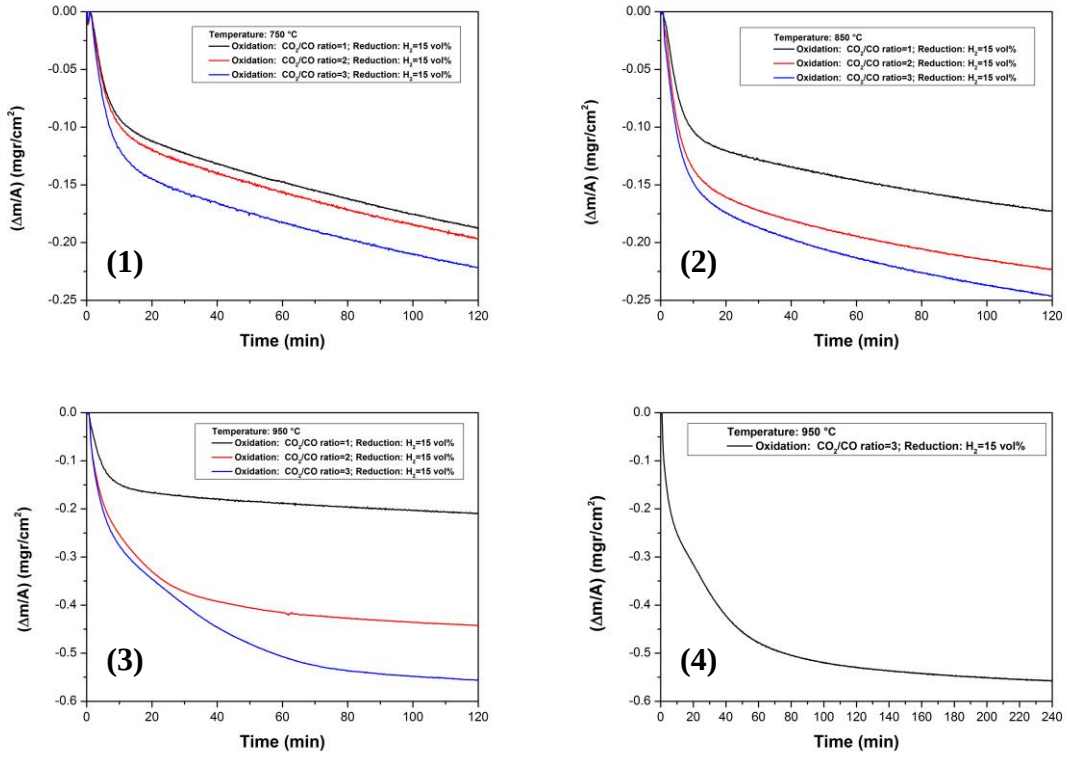

Figure 26 Reduction of the oxide layers by 15 vol% H_2 at the different temperatures in different CO_2/CO mixtures: (1)750 ℃, 2hours (2) 850 ℃, 2 hours (3) 950 ℃, 2 hours (4) 950 ℃, 4 hours

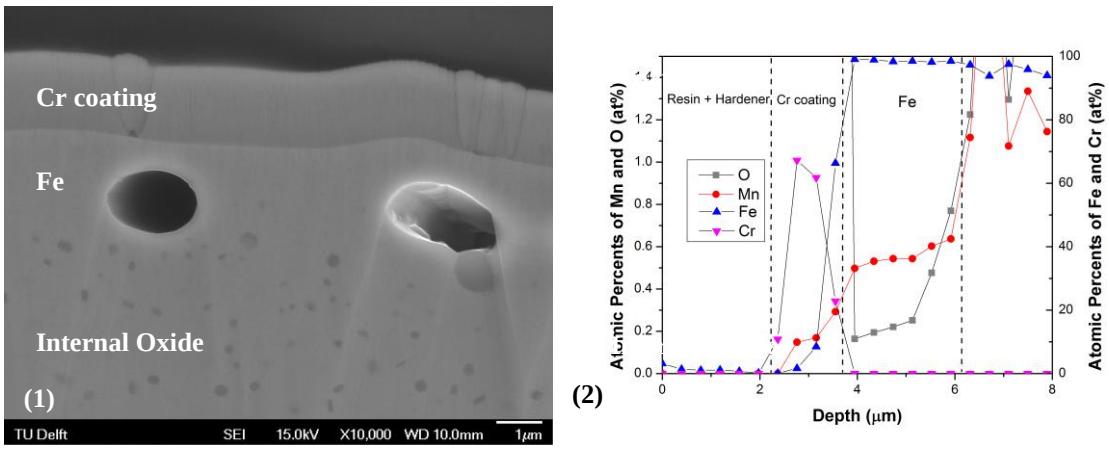

Figure 27 (1) cross-section of the sample oxidized in $CO_2/CO = 3$ at 950℃, then reduced for 2 hours by 15 vol% H_2; (2) EPMA result of Figure (1)

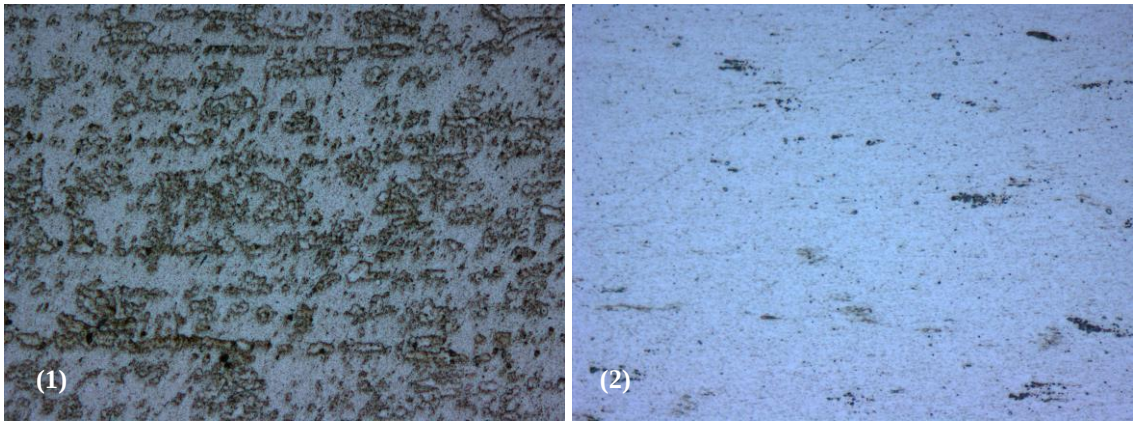

Figure 28 Cross-section of samples after etching with Nital (1 vol% Nitric acid+ethanol) (1) the cross-section of an original sample after annealing in 950℃ (2) cross-section of an sample oxidized in $CO_2/CO = 3$ at 950℃, then reduced by 15 vol% H_2 for 4 hours

The decarburization leads to difficulty in finding the end of the oxide reduction. To find the time that the oxide reduction is ended, the following data analysis is carried out. Consider the sample, which was oxidized in $CO_2/CO = 3$ at 750 ℃ and reduced for 2 hours by 15 vol% H_2, as an example. A parabolic relation is observed as shown in Figure 29. If it is assumed that (1) the mechanism of the decarburization does not change during the reduction experiment and (2) the decarburization occurs after the iron oxide reduction is finished, then the point where the linear fit deviates from the parabolic part of the reduction curve, can be defined as the reduction ending point; see Figure 29.

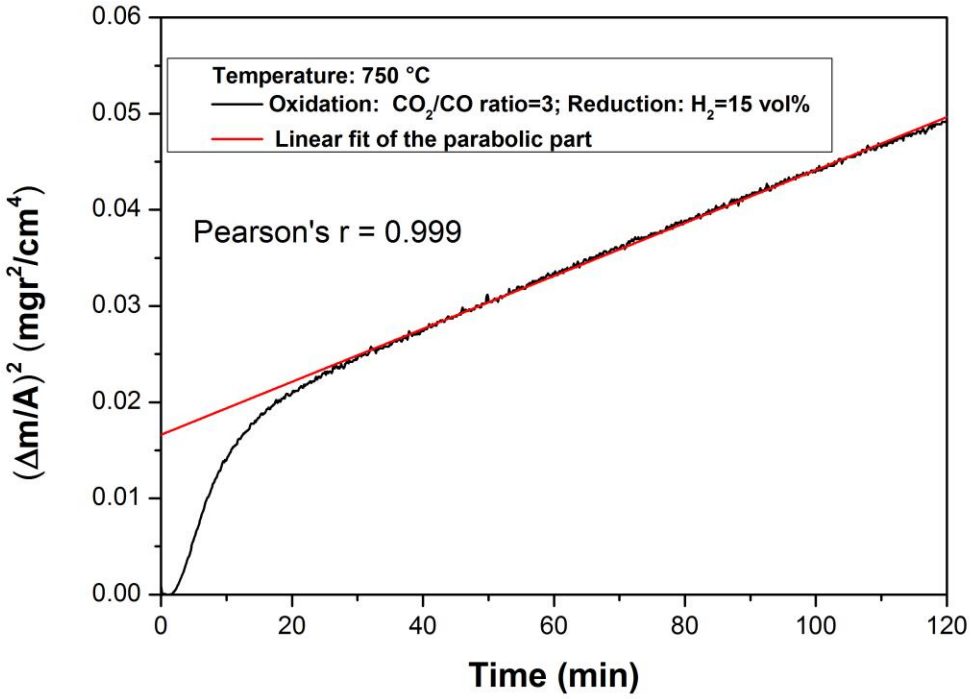

Figure 29 The parabolic relation in the decarburization process in a sample oxidized in $CO_2/CO = 3$ at 750 ℃ and reduced for 2 hours by 15 vol% H_2

Not all the decarburization follows a parabolic relation with time. The values for the exponent n in the equation $(\Delta m/A)^n = kt$ in the decarburization processes are shown in Table 13. Because the decarburization process is not the aim of this project, no further analysis will be considered.

Ratio\Temperature	**750**℃	**850**℃	**950**℃
$CO_2/CO = 1$	2	3	5
$CO_2/CO = 2$	2	4	-
$CO_2/CO = 3$	2	4	-

Table 13 Exponent value n in Equation $(\Delta m/A)^n = kt$ in decarburization process

After the determination of the endpoint of the oxide reduction, the oxide reduction part without the decarburization part is shown in Figure 30-(1). The reduction process is obviously a decelerating process and a first-order model fits the data; see Figure 30-(2).

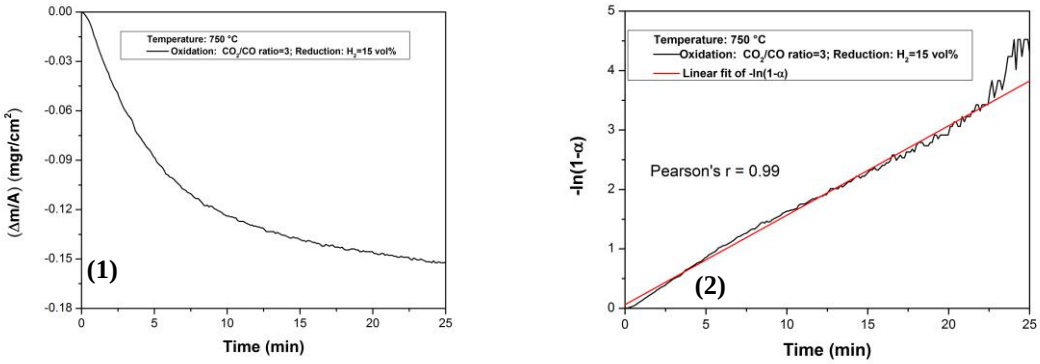

Figure 30 (1) the reduction reaction of the sample oxidized in $CO_2/CO = 3$ at 750 ℃ and reduced by 15 vol% H_2 at 750 ℃ (2) plots of $-\ln(1-\alpha)$ versus time using the data in figure (1)

The first-order model is also applicable to the other reduction experiments, except for two samples: (1) the sample oxidized in $CO_2/CO = 3$ at 950℃ and then reduced for 2 hours by 15 vol% H_2 and (2) the sample oxidized in $CO_2/CO = 2$ at 950℃ and then reduced for 2 hours by 15 vol% H_2.
The reduction kinetic can be described with Equation (2.41) and Equation (2.42):

$$\frac{d\alpha}{dt} = k(T)(1-\alpha)P_{H_2}^{n} \tag{2.46}$$

Since the partial pressure of hydrogen is constant (15 vol% H_2), the integral form of Equation (2.46) can be written as:

$$k'(T)t = -\ln(1-\alpha) \tag{2.47}$$

The value of k' is summarized in Table 14.

Ratio\Temperature	750℃	850℃	950℃
$CO_2/CO = 1$	0.164	0.252	0.241
$CO_2/CO = 2$	0.198	0.134	-
$CO_2/CO = 3$	0.151	0.122	-

Table 14 k' values in the different reduction experiments

However, every reduction experiment has different amount of iron oxide and oxide morphology: see Section 4.1.2. So every experiment has different pre-exponential factor A in the Equation (2.43). Therefore, the activation energy in Equation (2.43) is not calculated.

4.2.3 Internal oxidation in reduction

The depth of internal oxidation zone after the reduction is compared with the depth of internal oxidation zone after the oxidation in Table 15. The depths increase by 1~2 μm

after the reduction. Thus, also the internal oxidation occurs during reduction. Figure 31 shows no significant difference between the depths after the reduction for 2 hours and the reduction for 4 hours at 950 ℃. That means the internal oxidation zone does not grow after the reduction reaction. Thus, the internal oxidation should occur during the reduction reaction. The mechanism will be explained in Section 4.2.4.

Temperature	Experiment	$\frac{CO_2}{CO} = 1$	$\frac{CO_2}{CO} = 2$	$\frac{CO_2}{CO} = 3$
750 ℃	**Oxidation**	3.18 μm	2.70 μm	2.40 μm
	Reduction		4.28 μm	4.52 μm
850 ℃	**Oxidation**	11.62 μm	12.09 μm	12.33 μm
	Reduction	13.24 μm	14.04 μm	14.30 μm
950 ℃	**Oxidation**		13.83 μm	13.92 μm
	Reduction	16.18 μm	16.18 μm	16.79 μm

Table 15 Compare the internal oxidation depths in the oxidation and the reduction

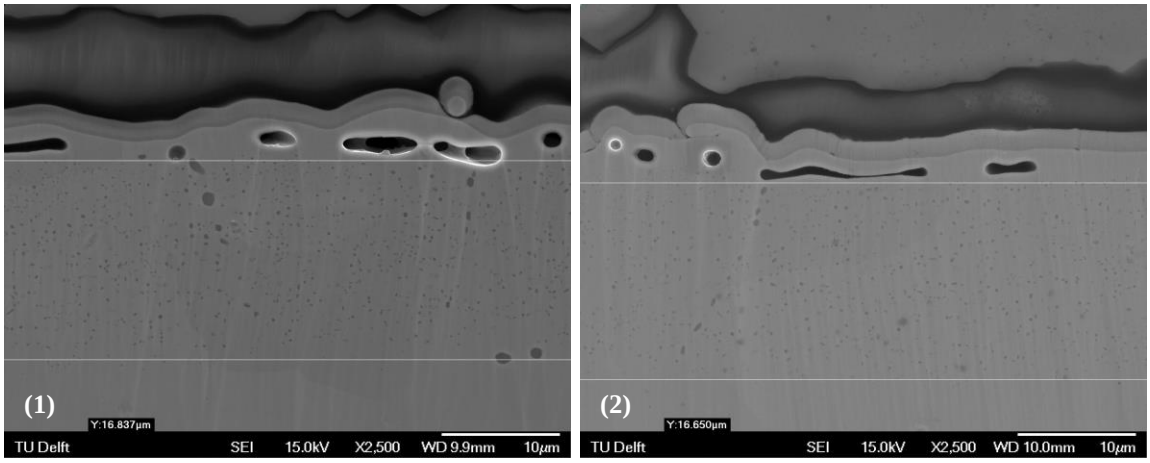

Figure 31 Cross-section of the samples oxidized in $CO_2/CO = 3$ at 950 ℃ and reduced at 950 ℃ by 15 vol% H_2 for different times (1) reduced for 2 hours (2) reduced for 4 hours

4.2.4 Reduction mechanism

The oxide reduction mechanism is described in Section 2.5. During the reduction, oxygen in the iron oxide diffuses to the surface and forms water vapor with hydrogen. The vacancies generated by the removed oxygen combine together to form the vacancy clusters or voids as shown in Figure 27 and Figure 31. The exceeded iron in the oxide/iron interface will precipitate, so that the iron grows inwards perpendicular to the surface.

In Section 4.2.3, the depths of the internal oxide zone increase by 1~2 μm during the reduction reaction. However, there are two possible mechanisms for this increasing depth. One is the oxygen diffuse to the alloy/internal oxide interface and react with manganese. The other mechanism is that manganese oxide precipitates at the oxide/internal oxide

zone interface when the iron grows outwards perpendicular to the surface. Two analysis results support the later mechanism.

(1) The thicknesses of the iron layers after the reduction are less than that of the oxide layers. A continuous oxide layer (~1 μm) is found in Figure 32-(1). However, after the reduction, the internal oxide zone reaches the surface as shown in Figure 32-(2) and (3). It proves that the internal oxide zone grows outward to the surface.

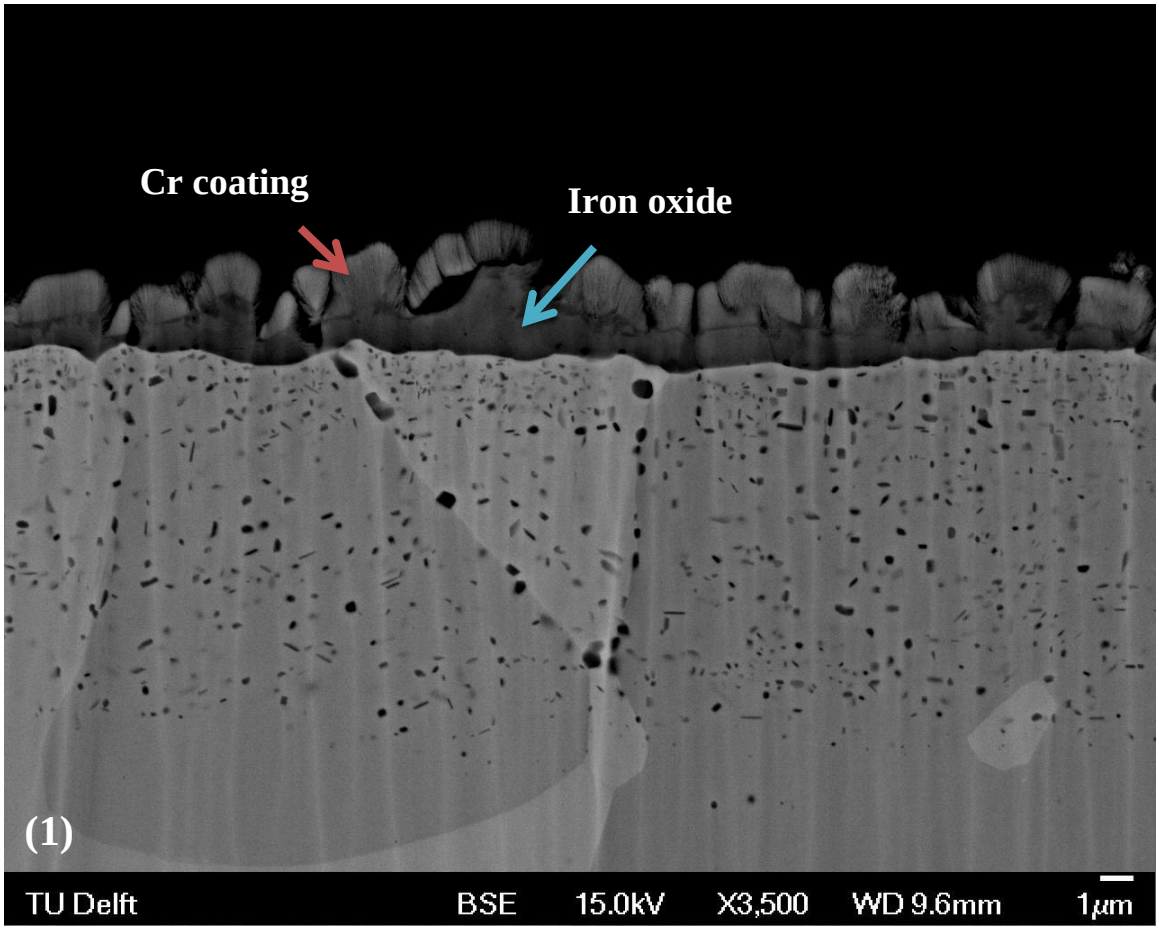

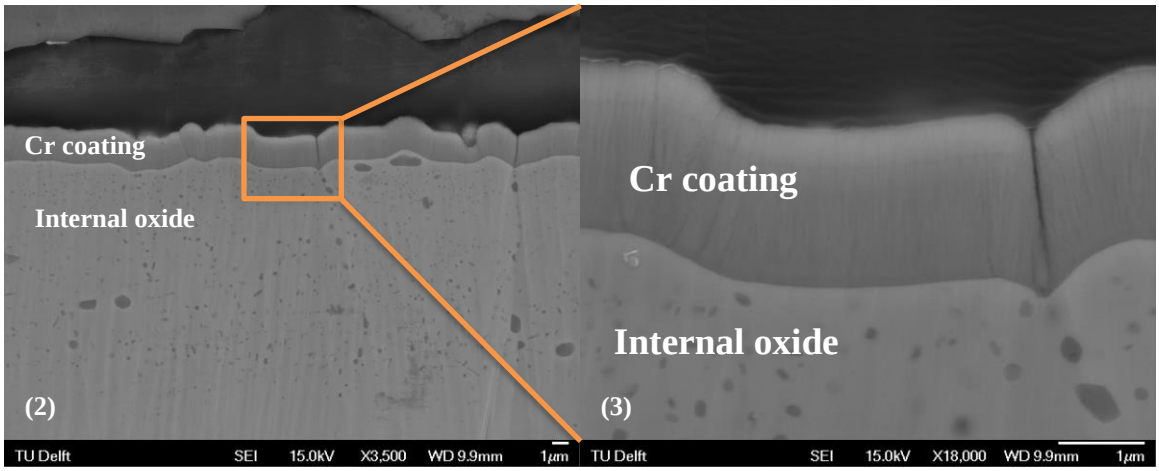

Figure 32 Cross-section of the samples (1) the sample oxidized in $CO_2/CO = 1$ at 850 ℃ (2) the sample oxidized in $CO_2/CO = 1$ at 850 ℃ and reduced by 15 vol% H_2 at 850 ℃ (×3500) (3) the sample oxidized in $CO_2/CO = 1$ at 850 ℃ and reduced by 15 vol% H_2 at 850 ℃ (×18000)

(2) The Manganese concentration in the oxide layer is less than that in the reduced iron layer. EPMA results in Figure 33 show the Mn concentration in the external scale is about 1.25 at.% and the concentration reduces to 0.48 at% after the reduction process. Thus, the lower of manganese concentration is caused by manganese oxide precipitation during the outward growth of the internal oxide zone.

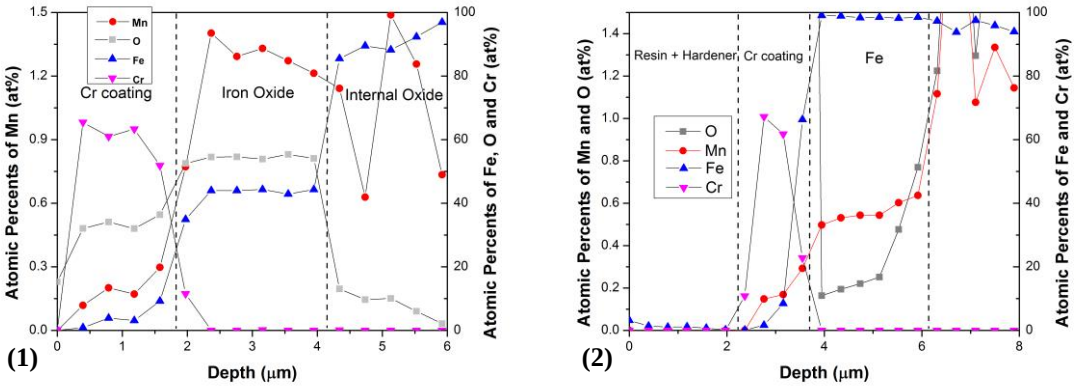

Figure 33 EPMA results of the samples (1) the sample oxidized in $CO_2/CO = 3$ at 950 ℃ (2) the sample oxidized in $CO_2/CO = 3$ at 950 ℃ and reduced by 15 vol% H_2 at 950 ℃

From two analysis results mentioned above, it can be concluded that manganese in the oxide layer precipitates as manganese oxide during the reduction reaction. Since manganese has high affinity with oxygen, The manganese element accumulates to the iron oxide as described in Section 4.1.5. During the reduction, when an iron layer is formed after reduction by hydrogen as shown in Figure 34, the manganese solute will diffuse to the unreduced iron oxide. Thus, as the iron layer grows and the oxide layer reduces, the manganese concentration becomes higher and higher in the oxide layer. At last, when the concentration of manganese reaches a critical value, manganese oxide

precipitates. If the manganese concentration is relatively low in the oxide layer before the reduction, the manganese oxide precipitates with a small size as shown in Figure 32-(3). If the manganese concentration is relatively high, large internal manganese oxides precipitate, as shown in Figure 25-(1). Thus the internal oxide zone grows outward perpendicular to the surface during oxide reduction.

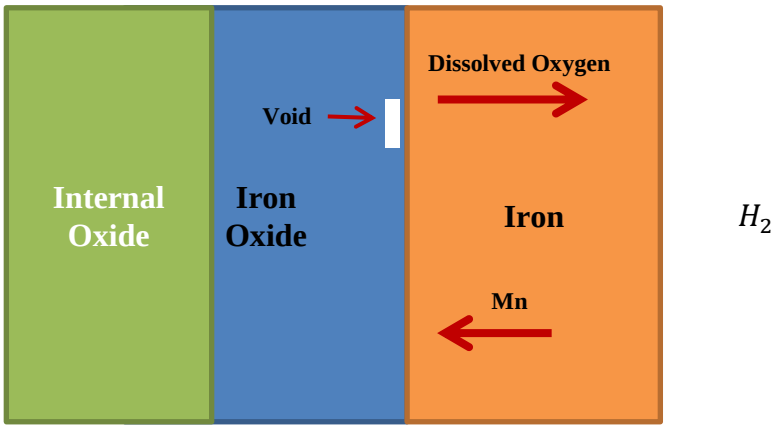

Figure 34 Schematic of the reduction process

5. Conclusion

In this thesis, an expected result as shown Figure 2 is obtained. In the oxidation experiment Manganese is fixed in the sub-surface and iron oxides cover the surface. In the reduction experiment, a pure iron surface is obtained for the Zinc coatings. Some other conclusions are summarized as below:

(1) Magnetite precipitates out during the cooling of Wüstite.

(2) In the oxidation experiments, the weight gains starts with a logarithmic growth then transit to a linear growth. In the logarithmic growth, the oxidation rate is controlled by electrical flow from the metal to the oxide. In the linear growth at 950 ℃, the dissociation of CO_2 into CO and adsorbed oxygen atoms or ions determines the oxidation rate.

(3) The depths of the internal oxide zone in the oxidation has higher values than the calculated value by Wagner's theory, because of the diffusion enhanced by the grain boundaries

(4) The surface of sample reduced by hydrogen has a high-concentration iron surface without external oxides.

(5) Decarburization occurs during the reduction by hydrogen.

(6) The Fist-Order model can apply to the Wüstite reduction by Hydrogen except the sample oxidized in $CO_2/CO = 3$ at 950 ℃ and the sample in $CO_2/CO = 2$ at 950 ℃.

(7) The depths of the internal oxide zone increase during the reduction reaction, because of the precipitation of alloy element oxide.

(8) The internal oxide zone grows outward perpendicular to the surface during the reduction.

6. Bibliography

[1] S. Klein and G. Nellis, Termodynamics, Combridge University Press, 2012.

[2] D. Young, High temrature oxiation and corrosion of metals, Elsevier, 2008.

[3] C. B. Carter and M. G. Norton, Ceramic Materials, Springer, 2007.

[4] E. McCafferty, Introduction to Corrosion Science, Springer, 2010.

[5] P. Sarrazin, A. Galerie and J. Fouletier, Mechanicsms of High temperature corrosion-a Kinetic approach, Trans Tech Publications Ltd, Switzerland, 2008.

[6] F. Kröger and H. Vink, "Relations between the Concentrations of Imperfections in Crystalline Solids," *Solid State Physics,* vol. 3, p. 307, 1956.

[7] H. H. Uhlig, "Initial oxidation rate of metals and the logarithmic eqation," *Acta Metallurgica,* vol. 4, p. 541, 1956.

[8] F. Pettit and J. Wagner, "Transition from the linear to the parabolic rate law during the oxidation of iron to wüstite in CO-CO2 mixtures," *Acta Metallurgica,* vol. 12, p. 35, 1964.

[9] F.Pettit, R.Yinger and J. J.B.Wagner, "The mechanism of oxidation of iron in carbon monoxide-carbon dioxide mixtures," *Acta Metallurgica,* vol. 8, p. 617, 1960.

[10] R. Bredesen and P. Kofstad, "On the Oxidation of Iron in CO2+CO Mixtures: II. Reaction Mechanisms During Initial Oxidation," *Oxidation of Metals,* vol. 35, p. 107, 1991.

[11] C.Wagner, "Reaktionstypen bei der Oxydation von Legierungen," *Zeitschrift fur Elektrochemic,* vol. 63, no. 7, p. 772, 1959.

[12] D.Ugur, A.J.Storm, R.Verberk, J.C.Brouwer and W.G.Soof, "Kinetics of reduction of a RuO2(110) film on Ru(0001) by H2," *The Journal of Physics Chemistry C,* vol. 116, p. 26822, 2012.

[13] M. Farren, S. Matthew and P. Hayes, "Reduction of Solid Wustite in H2/H2O/CO/CO2 gas mixture," *Metallurgical Transactions B,* vol. 21, p. 135, 1990.

[14] S.P.Natthew, T.R.Cho and P.C.Hayes, "Mechanisms of Porous Iron Growth on Wustite and Magnetite during Gaseous Reduction," *Metallurgical transactions B,* vol. 12, p. 733, 1990.

[15] D. S. Hohn, S. Matthew and P. Hayes, "The breakdown of dense iron layers on Wustite in CO/CO2 and H2/H2O systems," *Metallurgical Transactions B,* vol. 15, p. 701, 1984.

[16] S. Vyazovkin, A. K. Burnham, J. M. Criado and L. A. Perez-Maqueda, "ICTAC Kinetics Committee recommendations for performing kinetic computations on thermal analysis data," *Thermochimica Acta,* vol. 520, pp. 1-19, 2011.

[17] A. Khawam and D. R.Flanagan, "Solid-State Kinetics Models: Basics and Mathematical Fundamentals," *Journal of Physical Chemistry B,* vol. 110, pp. 17315-17328, 2006.

[18] N. Birks, G. H.Meier and F. S.Pettit, Introduction to the high-temperature oxidation of metals, Cambridge University Press, 2006.

[19] W. Smeltzer, "The kinetics of wustite scale formation on iron," *Acta Metallurgica,* vol. 8, p. 377, 1960.

[20] F.Gesmundo and F.Viani, "Transition from internal to external oxidation for binary alloys in the presence of an outer scale," *Oxidation of Metals,* vol. 25, p. 269, 1986.

[21] S.W.Guan, H.C.Yi and W.W.Smeltzer, "Internal oxidation of ternary alloys. Part II: Kinetics in the presence of an external scale," *Oxidation of Metals,* vol. 41, p. 389, 1994.

[22] F. Maak, "Zur Auswertung von Messungen der".

[23] F. Maak, "Zur Auswertung von Messungen der schichtdicken binarer Legierungen mit innerer Oxydation bei gleichzeitiger auberer Oxydation," *Z.Metallkde,* vol. 52, no. 8, p. 545, 1961.

[24] H.A.Wriedt, "The Fe-O (Iron-Oxygen) System," *Journal of Phase Equilibria,* vol. 12, p. 170, 1991.

[25] A.S.Khanna, High temperature oxidation and corrosion, ASM international, 2002.

7. Appendix

Appendix A: XRD results

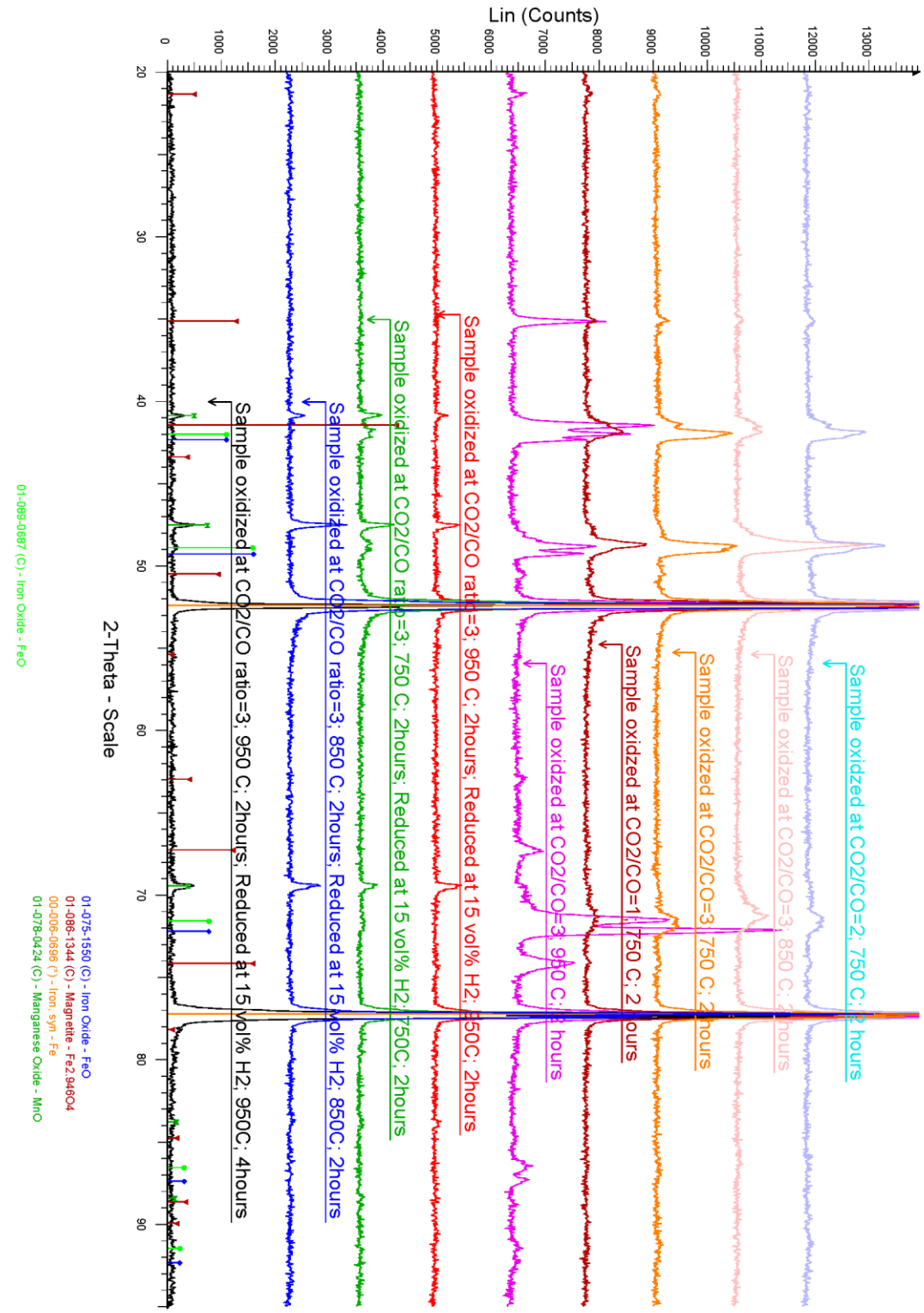

Appendix B: Data Used to calculate the internal oxide zone depth

The data used in Equation (2.30): $\frac{N_O^{(S)}}{vN_B^{(0)}} = \frac{\exp(\gamma^2)erf(\gamma)}{\phi^{1/2}\exp(\gamma^2\phi)erfc(\gamma\phi^{1/2})}$

, where $\gamma = (\frac{k_p^{(i)}}{2D_O})^{1/2}$ and $\phi = \frac{D_O}{D_B}$.

Diffusion coefficient of *Mn* in *Fe*-1.7wt% *Mn* alloy

Temperature	Diffusion coefficient ($\times 10^{-16}\ m^2/s$)	Reference
750 ℃	2.049	*Thermo-Calc*
850 ℃	36.0789	*Thermo-Calc*
950 ℃	1.142	*Thermo-Calc*

Gibbs free energy Data

Reaction	$\Delta G^0 = A + BT\ (J/mol)$		Reference
	A (*kJ/mol*)	B (*J/mol/K*)	
$Fe + \frac{1}{2}O_2 = FeO$	-264.89	65.4	A [1]
$Mn + \frac{1}{2}O_2 = MnO$	-412.3	72.8	A [1]
$CO + \frac{1}{2}O_2 = CO_2$	-282.4	86.8	A [1]

Oxygen dissolution in iron

Metal	$\Delta G^0 = A + BT\ (J/mol)$		Reference
	A (*kJ/mol*)	B (*J/mol/K*)	
$\alpha - Fe$	-155.6	42.69	A [2]
$\gamma - Fe$	-175.1	72.8	A [2]

Oxygen diffusion coefficient

$$D = D_0 \exp(\frac{-Q}{RT})$$

Metal	Temperature (*K*)	$D_0(\times 10^{-4}\ m^2/s)$	$Q\ (kJ/mol)$	Reference
$\alpha - Fe$	1023-1123	$1.79^{+1.76}_{-0.89} \times 10^{-3}$	85.7±6.1	
$\gamma - Fe$	1224-1623	5.754	166.8	

Appendix References

[1] D. Young, High temrature oxiation and corrosion of metals, Elsevier, 2008 Page 33
[2] D. Young, High temrature oxiation and corrosion of metals, Elsevier, 2008 Page 47

Acknowledgements

The success of any project depends largely on the encouragement and guidelines of many others. I would like to gratefully acknowledge the enthusiastic supervision of Dr. Ir. W.G.Sloof during this Thesis. He always can offer great ideas in the research and help me to understand everything clearly when I was confused. Special thanks to Hans Brouwer, who used 3 months to help me improve the experiment equipment. Vahid Aghaei Lashgari is thanked for his experiment instructions and the academic discussion with me. I also wish to express my thanks to Kees Kwakernaak, who always gave valuable support. I am grateful to Ruud Hendrikx and Niek van der Pers for their X-ray diffraction analysis.. I would like to thank all the group members especially Xi Zhang and Weichen Mao, my roommates and all who supported me.

Special thanks goes to Deayang Scholarship, which support me to study and have a great experience in the Netherlands. I am thankful to my family, who always gave me happiness and encourage to me. Last but not least I thank my girlfriend, Hannah Luo, for her support and understanding.